

Biogenically modified reservoir rock quality: A case from the lowermost member Paleocene Funing Formation, Gaoyou Depression, Subei Basin, China

Jonathan Ataquaye Quaye^{a,*}, Zaixing Jiang^b, Chao Liu^b, Caspar Daniel Adenutsi^a, Cyril Dziedzorm Boateng^c

^a Department of Petroleum Engineering, Faculty of Civil and Geo-Engineering, College of Engineering, Kwame Nkrumah University of Science and Technology, Kumasi, Ghana

^b School of Energy Resources, China University of Geosciences Beijing, No. 29 Xueyuan Road, Haidian, Beijing, 100083, China

^c Department of Physics, Faculty of Physical and Computational Sciences, College of Science, Kwame Nkrumah University of Science and Technology, Kumasi, Ghana

ARTICLE INFO

Keywords:
Biogenic
Gaoyou
Reservoir quality
Porosity
Permeability
Subei basin

ABSTRACT

Bioturbation can influence reservoir quality and is consequential to the producibility of a reservoir. The study of samples from the lowermost member of the Paleocene Funing Formation (E_1f_1), Gaoyou Depression, Subei Basin, shows how bioturbation affects reservoir quality. Techniques used to study the samples include petrography, pressure decay porosimetry, pulse decay permeametry, Field Emission Scanning Electron Microscopy, and Energy Dispersive X-ray Spectroscopy. Sample A is intensely burrowed by *Taenidium*, *Scoyenia*, *Skolithos*, *Palaeophycus*, and other trace fossils. Increased isotropy in sample A contributes to cleaner well-sorted burrows, relative to its surrounding matrix, and 67.18% augmented burrow porosity. *Taenidium* and *Palaeophycus* in sample B indicate 20.23% improved burrows porosity. Plant debris and/or root traces in sample C have a 3.68% reduction in porosity. In samples A and B, the arithmetic mean of permeability describes all horizontal fluid flows within burrows. In sample C, the geometric mean of permeability describes the fluid flow in all directions. Porosity is $\leq 11.2\%$, permeability ≤ 1 md in samples, and sample C log-derived porosity $\leq 0.33\%$. This study demonstrates that bioturbation together with depositional factors (sorting, grain size distribution, and mud-matrix/burrow content) and diagenetic modifications (albitization, compaction, dissolution, kaolinization, and precipitation) control the quality of the high to intensely bioturbated (Bioturbation Index 4 to 5; 61–99 vol %) sandstone and siltstone reservoir facies of the E_1f_1 .

1. Introduction

Burrowing activities by organisms alter textural characteristics and diagenetic effects of the substrate, which can result in partial or complete removal of occurring substrate structures and alter sorting (Bromley and Ekdale, 1984; Meadows and Tait, 1989; Green et al., 1992; Jensen and Bromley, 1996; Katrak and Bird, 2003; Bastardie et al., 2003). The burrows produced by these organisms contain sediments that are lithological and geochemically distinct from the matrix (Over, 1990; Konhauser and Gingras, 2011; Petrash et al., 2011). This outcome can increase or reduce burrow porosity and permeability contrasted with the surrounding matrix (e.g., Gingras et al., 1999; Gordon et al., 2010; Lemski et al., 2011; Baniak et al., 2013; La Croix et al., 2013; Baniak

et al., 2015; Ben-Awuah and Padmanabhan, 2015; Leaman and McIlroy, 2017; Baniak et al., 2022). Organism-substrate interaction has crucial control over reservoir quality. Thus the ichnological analysis of burrowed reservoir facies is key to reservoir characterization (Dey and Sen, 2017). Bioturbated siliciclastic reservoirs occur globally: the Upper Jurassic Fulmar Formation and Middle Jurassic Brent Group, North Sea, United Kingdom (Martin and Pollard, 1996); the Lower Cretaceous Ben Nevis Formation, Jeanne d'Arc Basin, offshore Newfoundland, Canada (Tonkin et al., 2010); the Lower Cretaceous Bluesky Formation, Alberta, Canada (Gordon et al., 2010); the Cycles VI and VI reservoir sandstones of the Baram Delta, Offshore Sarawak, Malaysia (Tan et al., 1999); and the Upper Jurassic Ula Formation, Norwegian North Sea, Europe (Baniak et al., 2015) to name a few.

* Corresponding author.

E-mail address: jonathanatuquayequaye@gmail.com (J.A. Quaye).

<https://doi.org/10.1016/j.petrol.2022.111126>

Received 29 January 2022; Received in revised form 25 September 2022; Accepted 10 October 2022

Available online 18 October 2022

0920-4105/© 2022 Elsevier B.V. All rights reserved.

Pemberton and Gingras (2005) proposed that two controls can cause biogenic-enhanced permeability: 1) burrow-associated alteration of fundamental depositional structures; and 2) diagenetic modification of sedimentary matrix through recrystallization. In the Funing Formation of the Subei basin, sandstone and siltstone reservoir heterogeneity is usually attributed to variations in depositional factors and diagenetic processes. The sedimentological heterogeneity in a reservoir causes the highly burrowed and permeable zones to alter pore connectivity and flow behaviour (Usman et al., 2020).

The Jiangsu Oilfield Company Ltd (SINOPEC) oversees thirty-eight (38) oil and gas fields in the Subei basin. As of 2011, the total proven reserve was more than 0.267 billion tons of crude oil and 8.518 billion m³ of natural gas (Liu et al., 2017). Sandstone and siltstone reservoirs in the Funing Formation comprise bioturbated horizons (see section 2.3). Foremost studies on bioturbation by Quaye et al. (2019) and Zhou et al. (2019) have described its effect on reservoir quality and characterized the ichnology and sedimentology in the Funing Formation, respectively. This study focuses on the depositional and diagenetic factors that control sandstone and siltstone reservoir quality in the lowermost member of the Paleocene Funing Formation (E₁f₁). The outcome may help identify ignored secondary reservoir targets and possibly augment reserve estimates in petroleum fields of the Gaoyou Depression.

2. Geological setting

Fig. 1A shows the Subei basin at the Yellow Sea's western border in the north of Jiangsu province, east China. It is a fault sag basin that began as a rift during the Late Cretaceous covering about 35,000 km² (Song et al., 2010). Two main rifts occurred from 83 to 54.9 Ma and 54.9 to 38 Ma (Yang and Chen, 2003; Chen, 2010). They were separated by

the Wubao and Sanduo tectonic events and were accompanied by thermal subsidence (Liu et al., 2014). The Wubao tectonic event resulted in intrabasinal faulting and partitioning (Liu et al., 2017). The Sanduo tectonic event caused major uplift and eventual erosion of the Oligocene and underlying strata (Yi et al., 2003), resulting in angular unconformity between the Neogene and underneath strata.

Located in the south of the Subei basin is the Gaoyou depression (Fig. 1B), which covers about 2670 km². From the east to the west, it spans more than 100 km and is about 30 km wide between the north and south. The Gaoyou depression is a half-graben and separated at the south and east by the Tongyang and Wubao Low uplifts. The depression is bounded by Jiangdu-Wubao fault zone, which extends over 140 km and includes the such significant faults as Zhen 1, Zhen 2, Wu 1, and Wu 2. There are four depocenters located within the Gaoyou depression: the Shaobo, Fanchuan, Liuwushe, and Liulu sub-basins (Liu et al., 2017).

On the west, the Gaoyou depression is bound by the Lingtangqiao Low Uplift. It is bound on the south by the Tongyang Uplift, on the east by the Wubao Low Uplift, and extends into the sag at the northeastern boundary by the Zheduo Low Uplift (Fig. 1C). During the Dainan-Yancheng period, two growth faults in the southern region of the Gaoyou depression moved to partition it into three members: 1) North Slope, 2) Central Deep Sag, and 3) South Fault-Terrace Belt (Gu and Dai, 2015).

2.1. Sedimentary background and stratigraphy

The lowermost member of the Funing Formation (E₁f₁) comprises storm deposits in hydrocarbon-rich lacustrine basins can be excellent reservoirs and interpretation of storm deposits have great significance for future petroleum exploration (Liu et al., 2021). Recent developments

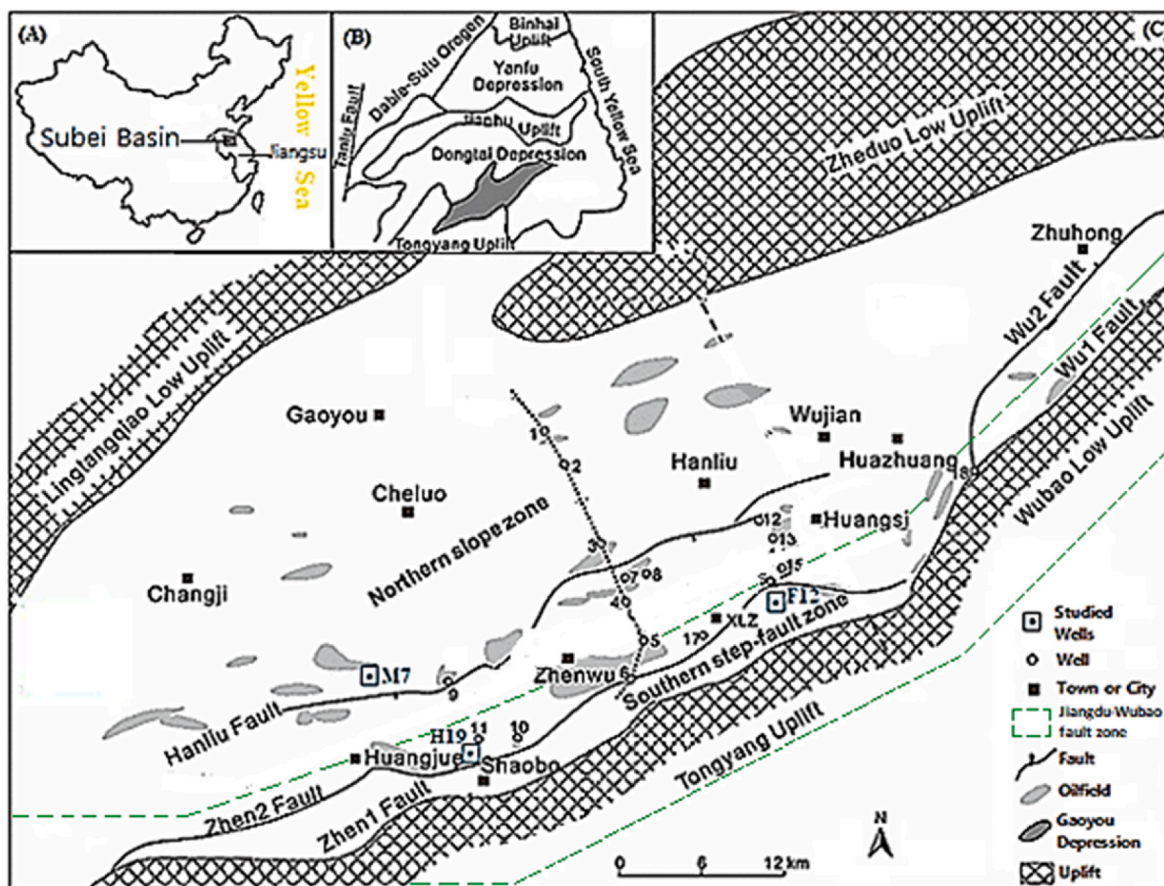


Fig. 1. (A) Location of the Subei Basin in Jiangsu, China; (B) location of the Gaoyou Depression in the Subei basin; (C) the Gaoyou Depression showing bounding tectonic units and well positions.

in facies analysis of the E₁f₁ show that weakly laminated or massive fine-grained sandstone and planar-laminated siltstone beds in a relatively deeper lacustrine setting are the results of collective gravity, unidirectional, and oscillatory flows (Dumas et al., 2005; Basilici et al., 2012).

From the youngest to oldest, the principal sedimentary formations in the Gaoyou depression are the Quaternary Dongtai Formation (Qd), Neogene Yancheng Formation (Ny), Eocene Sanduo (E₂s) and Dainan (E₂d) Formations, Paleocene Funing (E₁f) Formation, and Cretaceous Taizhou Formation (K₂t). They have a sedimentary thickness of 7000 m altogether (Zhang et al., 2004). The Pukou Group (K₂p), Chishan Group (K₂c), and Gecun Group (K₁g) are not considered principal sedimentary formations. The Oligocene was a period of erosion in the depression (Fig. 2; Zhu et al., 2013). The Funing Formation constitutes the first, second, third, and fourth members. The first, second, and third members comprise reservoirs, whereas the fourth member forms the most productive primary source rock (Chen et al., 2008; Gang et al., 2012; Jiang et al., 2014). Taizhou Formation thickness is between 150 and 400 m and is subdivided into the Upper and Lower Members (K₂ t₂, K₂ t₁). The Lower Member has brownish-grey sandstones interbedded with purplish-brown and grey shales that were deposited in a semi-deep lake and alluvial plain environment (Gao et al., 2018).

The lowermost member of the Paleocene Funing Formation i.e. the first member of the Funing Formation (E₁f₁) accumulated in a lacustrine environment during the first rifting phase (65–54.9 Ma) of the Gaoyou

depression and represents the most productive member (Xuming et al., 2016). The first member is between 350 and 800 m thick and has a 1000 m maximum thickness (Fig. 2). Lithology comprises siltstones, mudstones, and brownish-red, very fine-to fine-grained sandstones teeming with trace fossils, and an unequal interbedding of greyish-green, very fine-to fine-grained sandstones and siltstones (Zhang et al., 2006; Deng, 2014). The overlying member (E₁f₂) comprises interbedded lacustrine carbonates and grey, very fine-grained sandstone 70–110 m thick. Dark grey mudstone occurs as a source unit between 60 and 120 m thick (Liu et al., 2012; Luo et al., 2013; Shao et al., 2013). Member three (E₁f₃) comprises interbedded grey very fine-grained sandstones and grey mudstones 200–300 m thick, overlain by member four (E₁f₄). Member four consists of dark grey mudstone 300–400 m thick (Zhang et al., 2006). This research focuses on the bioturbated intervals from the lowermost member of the Funing Formation (E₁f₁), which contains vast ephemeral fluvial complexes with abundant trace fossils (Figs. 3A–1). The upper and lower parts of the formation have sandstones that are well developed with mudstones being relatively abundant mud in the middle section. The entire middle section contains thin layers of star-dispersed gypsum or gypsum-bearing mudstone. Gravel-bearing sandstones and even sandy-conglomerate layers (such as in Xuzhuang and Gonghe) have formed near the bottom of the basin margin. The underlying bottom section has gradational contact with the Taizhou Formation. In all formations, sandstone and shale are the principal lithologies in a continental river-lake environment.

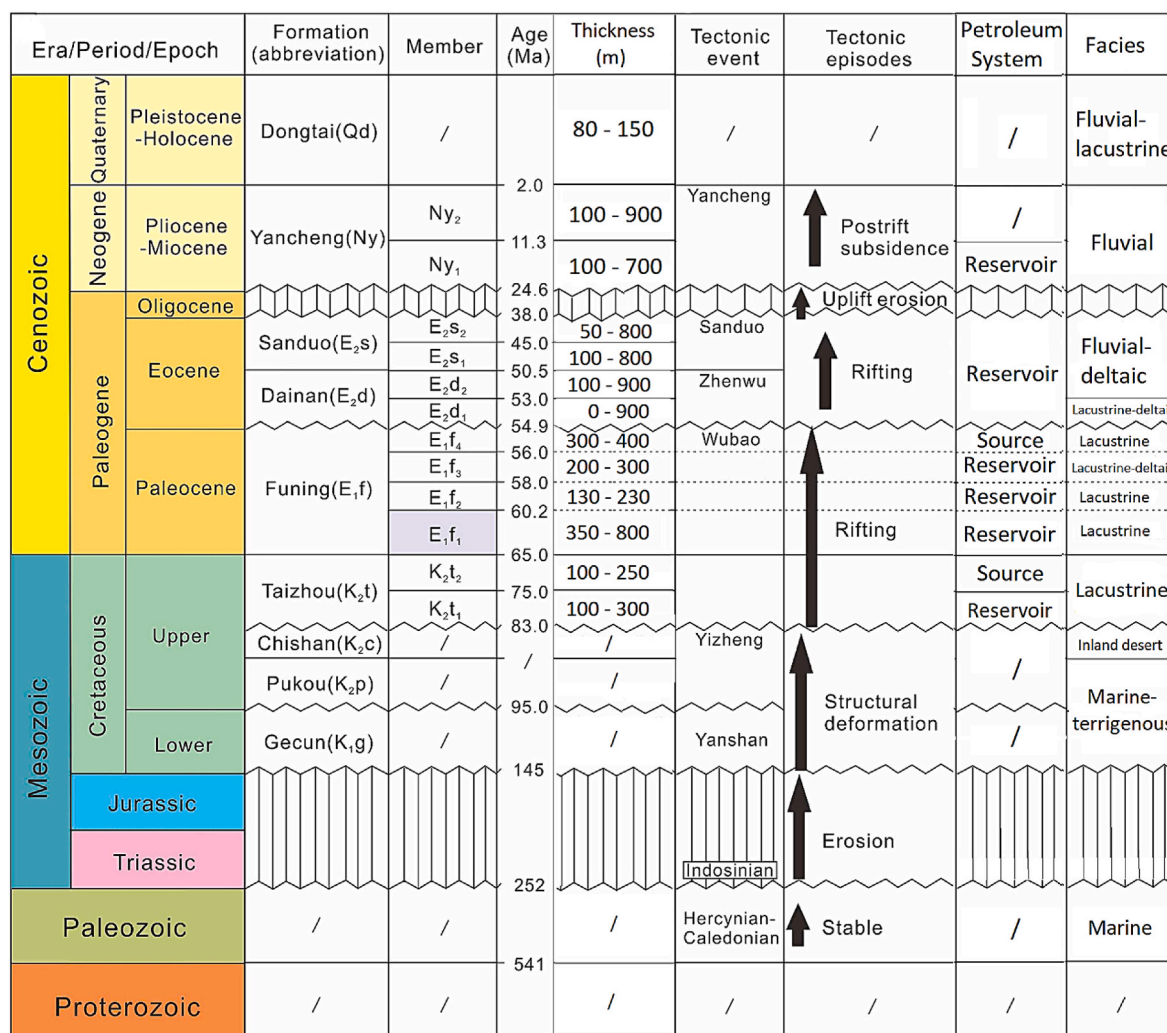


Fig. 2. Detailed stratigraphy, tectonic events, petroleum systems, facies, and evolution of the E₁f₁ - E₁f₄ (65.0–54.9 Ma). Modified after Zhou et al. (2019).

2.2. Optimizing production in “tight” E_{1f_1} reservoirs

The E_{1f_1} has characteristics of a typical low-permeability reservoir. The oil single-layer thickness ranges between 0.8 and 3.6 m, with the average permeability of the oil layer about 8.6 md. A detailed description of sedimentation, diagenesis, capillary pressure parameters, microscopic casting thin-film measurement data, and test results ascribes the E_{1f_1} as high quality (class 1) reservoir rock type with strong water sensitivity, strong salt sensitivity, moderately weak velocity-sensitive, and moderately weak soil acid-sensitive (Qin and Tang, 2003). Hydraulic fracturing has been used as a suitable technology to improve the production of Funing Formation reservoirs. From 1996 to 2002, twenty-seven reservoir wells achieved good results through hydraulic fracturing with an efficiency of 87%. By the end of 2002, the cumulative oil increase in the fractured wells was 254,040 B (Yan and He, 1994).

2.3. Ichnofauna description of the E_{1f_1}

The Subei basin was possibly situated in a semiarid setting in the early Paleocene with sporadic rainfall patterns and yielded moderately diverse ichnofauna (Zhou et al., 2019). Frequently reported in semiarid to arid regions affected by seasonal rainfall, past and present records of ephemeral fluvial red beds are linked to sporadic flood events. (e.g., Deluca and Eriksson, 1989; Dam and Andreasen, 1990; Allen et al., 2014; Knight and Evans, 2017; Horn et al., 2018).

The lowermost member of the Funing Formation comprises nine moderately distinct ichnotaxa of the *Scoyenia* ichnofacies that include meniscal burrows (*Beaconites coronus* (Fig. 3A), *Taenidium satanassi* (Fig. 3B), and *Taenidium barretti* (Fig. 3C)), simple horizontal cylindrical burrows (*Planolites isp* (Fig. 3D), *Palaeophycus heberti* (Fig. 3E), and *Palaeophycus tubularis* (Fig. 3F)), plant debris and/traces (Fig. 3G), and simple sub-vertical or vertical burrows (*Skolithos isp.* (Fig. 3H), and *Skolithos linearis* (Fig. 3I)). These ichnofossils predominantly occur in sandstones and siltstones of the E_{1f_1} (Zhou et al., 2019).

3. Methods and materials

The selection of three reservoir facies is based on availability, oil-fields wellbore orientation, dominant burrows, degree of bioturbation, absence of fissures/fractures, and any defect that could adversely affect test results. This study uses the Bioturbation Index (BI) which grades the degree of burrowing in sediments by organisms on a scale of zero to six (Taylor and Goldring, 1993) as seen in Table 1. The core samples A, B, and C from M7, F12, and H19 wells (Fig. 1C) of the Mjiazui, Fumin, and Huangjue oilfields, respectively. Sample A (20 × 11 × 5 cm) is intensely bioturbated (BI = 5; 91–99 vol %), fine-grained, brownish-red siltstone at 2104.98 m deep; sample B (16 × 11 × 5 cm) is highly bioturbated (BI = 4; 61–90 vol%), fine-grained, brown sandstone at 2071.47 m deep, and sample C (14 × 9 × 5 cm) is highly bioturbated (BI = 5; 61–90 vol %), fine-grained, yellowish-brown sandstone at 3095.45 m deep.

3.1. Thin-section petrography

From core-slab surfaces, thin-section specimens (4 × 5 × 0.1 cm) were cut. The specimens were treated with dyed epoxy resin to highlight pore spaces in different lights under the Carl Zeiss Axio Scope A1 microscope. Subsequently, intergranular porosity, grain sorting, size, distribution, trace fossil(s), and minerals and/or organic matter were analyzed under the plane and cross-polarized lights.

3.2. Pulse decay permeametry (PDP)

The Pulse Decay Permeameter 200 (PDP-200) measurements were collected from slabbed core surfaces at the China University of Geosciences (Beijing, China). It conveys a differential pressure through the

sample after saturating the sample to specific pore pressure. A computerized data acquisition system records the time, delta pressure and downstream pressure as the transient pressure extends through the sample. A screen that allows visual quality control of the permeability measurement displays in real-time a log differential pressure times mean pressure versus time plot. The PDP-200 represents an ultra-low permeability tester that measures between 1 and 10×10^{-6} millidarcies (md). It is an analogous way of measuring very low permeability in rocks.

3.3. Pressure decay porosimetry and permeametry

Equivalent air permeability, porosity (0.01–40%), sample length, sample diameter, and pore volume were measured by the Core Measurement System, Model 300 (CMS-300), Stage 4.00, automated computer-directed, integrated, and unsteady-state pressure decay permeameter and porosimeter. An advanced calibration procedure is combined with Boyle’s Law to execute measurements. This calibration method is an advanced algorithm that permits exact restrictive pressure to correspond to the imputed limiting pressure. This promotes the measurements’ accuracy. The CMS300-type computer-controlled, automatic pressure-infiltration test instrument measures pressure in simulated strata up to 10,000 PSIG and can test the porosity and permeability of rocks under different pressures. Samples A, B, and C yielded 18 plugs (Table 2), 9 plugs (Table 3), and 4 plugs (Table 4), respectively. Each porosity data point was measured twice, and the discrepancy between values greater than 1% was averaged. The CMS 300 and PDP-200 corresponding permeabilities were averaged to obtain a typical permeability value.

3.4. Acoustic wireline log-derived porosity

The acoustic porosity (equation (1)) of a 2 m (i.e., 3094.125–3096.125 m) interval that intersects the position of sample C is calculated using Wyllie’s equation:

$$\varnothing = \frac{\Delta t - \Delta t_{ma}}{\Delta t_f - \Delta t_{ma}} \quad (1)$$

- (1) Δt_{ma} is the acoustic transit time of the rock matrix ($\mu\text{sec}/\text{m}$), Δt_f is the acoustic transit time of interstitial fluids ($\mu\text{sec}/\text{m}$), and Δt is the acoustic transit time ($\mu\text{sec}/\text{m}$). Precise values for Δt obtained from an acoustic log are shown in Table 5 in $\mu\text{sec}/\text{m}$; Δt_f is 656.168 $\mu\text{s}/\text{m}$ (water with 15% NaCl); Δt_{ma} is 172.572 $\mu\text{s}/\text{m}$ (for consolidated sandstone). The estimated acoustic porosities are compared to the core-derived laboratory porosities.

3.5. Framework for explaining permeability relationships

Three methods (arithmetic, geometric and harmonic) are used to calculate average permeabilities in a homogeneous system (Freeze and Cherry, 1979; Warren and Price, 1961; Weber and van Geuns, 1990). The arithmetic mean defines horizontal fluid flows in the most permeable media (e.g. along burrows; Gingras et al., 1999). The harmonic mean applies to vertical fluid flows in permeable units (e.g., across burrows). The geometric mean defines fluid flows in all directions in porous media. Thus the harmonic and arithmetic means reflect the numerical evaluation of bulk permeability (Renard and De Marsily, 1997).

Freeze and Cherry (1979) describe the arithmetic-mean permeability (equation (2)) as the average permeability in rocks that have layered parallel beds with different permeabilities:

$$k_{\text{arithmetic}} = \sum_{i=1}^n \frac{k_i d_i}{d} \quad (2)$$

where k_i is the permeability of each layer, d_i is the thickness of every single layer, and d is the overall thickness. The harmonic-mean

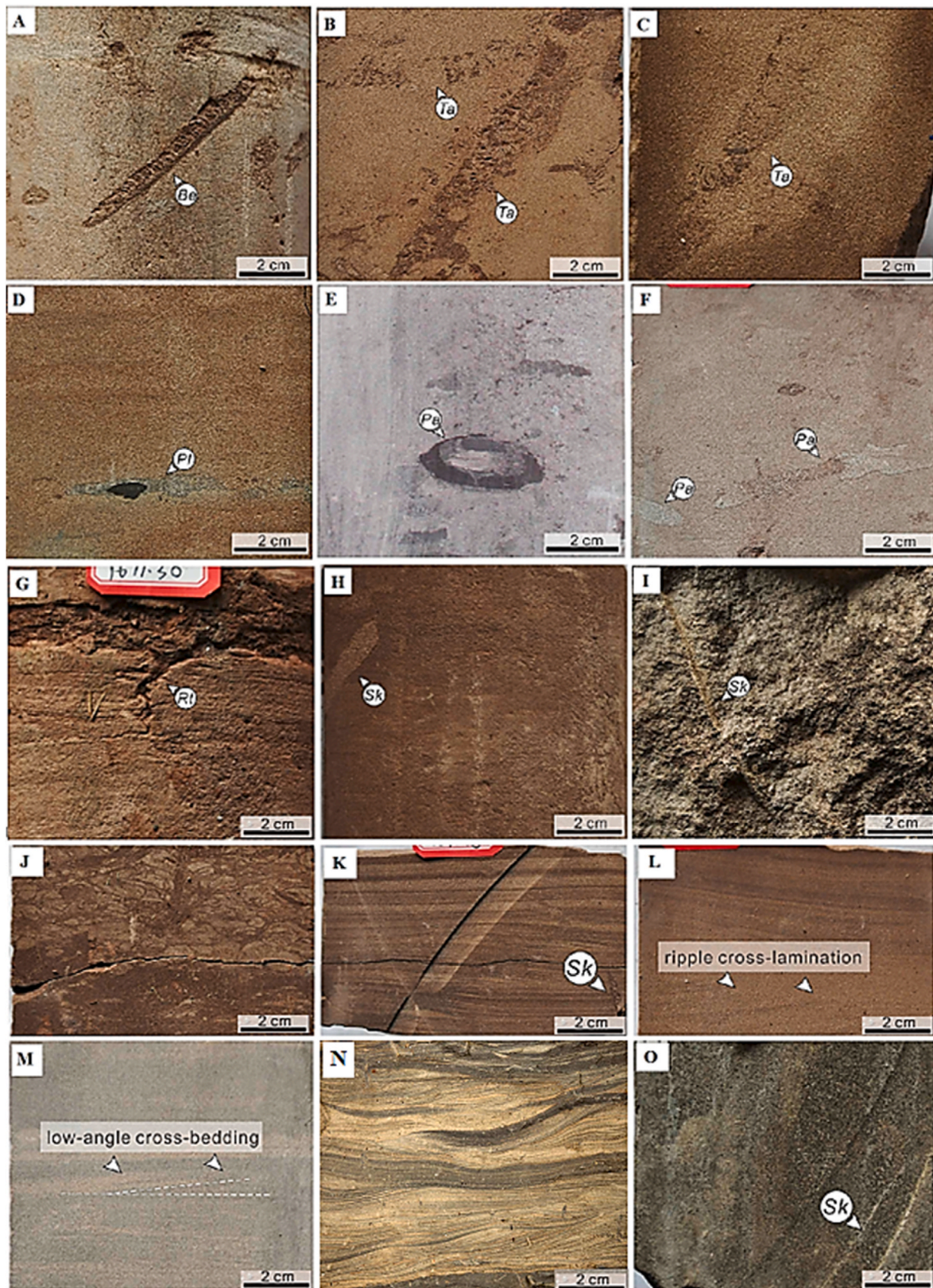


Fig. 3. Selected examples of burrows and structures in cores from wells M7, F12, and H19 in the lowermost member Paleocene Funing Formation. (A) *Beaconites coronus* (Be); (B) *Taenidium satanassi* (Ta); (C) *Taenidium barretti* (Ta); (D) *Planolites* isp. (Pl); (E) *Palaeophycus heberti* (Pa); (F) *Palaeophycus tubularis* (Pa); (G) plant debris and/traces (Rt); (H) *Skolithos* isp. (Sk); (I) *Skolithos linearis* (Sk); (J) silty flow rolls; (K) parallel-lamination with *Skolithos linearis*; (L) ripple cross-lamination; (M) low-angle cross-bedding; (N) hummocky cross Stratification; (O) massive structure with *Skolithos* isp.

Table 1
Bioturbation Index (BI) – a blueprint employed to quantitate the degree of sediment bioturbation. Modified after Taylor and Goldring (1993).

Bioturbation Index (BI)	Percent (%) Bioturbated	Classification
0	0	No bioturbation
1	1–4	Disperse bioturbation, apparent bedding with little separate traces or escape structures
2	5–30	Low bioturbation, apparent bedding, low trace density and escape structures mainly common
3	31–60	Moderate bioturbation, exact bedding boundaries, separate traces and rare overlap
4	61–90	High bioturbation, weak bedding boundaries and high trace density with regular overlap
5	91–99	Intense bioturbation, entirely interrupted bedding (just visible), limited reworking and later burrows discontinuous
6	100	Complete bioturbation and sediment reworking as a result of continuous overprinting

permeability (equation (3)) is the bulk vertical permeability perpendicular to the layered media:

$$k_{\text{harmonic}} = \frac{1}{\sum_{i=1}^n \frac{d_i}{k_i d}} \quad (3)$$

Table 2
Sample A petrophysical properties (CMS-300 and PDP-200).

Sample Length (cm)	Sample Diameter (cm)	Sample Vol. (cm ³)	Dry Wt. (g)	Particle Size (cm ³)	Pore Vol. (cm ³)	Porosity (%)	Vol. Density (g/cm ³)	Particle Density (g/cm ³)	Permeability (md)	Location
2.146	2.528	10.766	26.84	10.06	0.7015	6.5122	2.49	2.67	0.016	Burrow
4.246	2.526	21.267	53.86	20.52	0.7446	3.4995	2.53	2.62	0.0156	Burrow
2.394	2.524	11.972	30.28	11.52	0.4557	3.8041	2.53	2.63	0.035	Burrow
2.384	2.538	12.055	30.57	11.12	0.9343	7.7463	2.54	2.75	0.0246	Burrow
4.142	2.536	20.911	52.22	19.28	1.6342	7.8109	2.5	2.71	0.0241	Matrix
1.946	2.532	9.794	24.35	8.8	0.9977	10.1828	2.49	2.77	0.0123	Burrow
2.218	2.518	11.039	28.07	10.15	0.8923	8.0784	2.54	2.77	0.0282	Burrow
4.14	2.528	20.769	52.71	19.47	1.2974	6.2435	2.54	2.71	0.0214	Burrow
2.446	2.534	12.329	30.76	11.71	0.6172	5.0032	2.49	2.63	0.0347	Burrow
2.206	2.528	11.067	27.61	10.52	0.5508	4.974	2.49	2.63	0.036	Burrow
4.24	2.534	21.372	54.41	19.96	1.4081	6.5851	2.55	2.73	0.021	Burrow
2.1	2.528	10.535	26.11	9.56	0.9717	9.219	2.48	2.73	0.0358	Burrow
2.232	2.532	11.233	27.76	9.96	1.2723	10.03	2.47	2.79	0.0091	Burrow
4.552	2.522	22.728	57.16	21.17	1.562	6.869	2.51	2.7	0.0200	Matrix
2.308	2.536	11.652	28.72	10.68	0.9736	8.3514	2.46	2.69	0.0119	Burrow
1.95	2.528	9.783	24.59	9.27	0.5152	5.2636	2.51	2.65	0.0091	Matrix
3.53	2.538	17.85	45.24	16.87	0.9766	5.4682	2.53	2.68	0.0133	Burrow
2.388	2.524	11.942	29.73	11.24	0.7022	5.8771	2.49	2.65	0.0561	Burrow

Table 3
Sample B petrophysical properties (CMS-300 and PDP-200).

Sample Length (cm)	Sample Diameter (cm)	Sample Vol. (cm ³)	Dry Wt. (g)	Particle Size (cm ³)	Pore Vol. (cm ³)	Porosity (%)	Vol. Density (g/cm ³)	Particle Density (g/cm ³)	Permeability (md)	Location
1.716	2.518	8.541	20.49	8.01	0.5324	6.2307	2.4	2.56	0.3674	Burrow
3.708	2.528	18.602	44.53	17.37	1.2316	6.6175	2.39	2.56	0.455	Burrow
1.676	2.514	8.315	19.75	7.56	0.7533	9.0549	2.38	2.61	0.9349	Matrix
1.334	2.534	6.724	15.66	6.6	0.1201	1.7847	2.33	2.37	0.4474	Matrix
3.908	2.52	19.482	47.22	17.61	1.8669	9.578	2.42	2.68	0.2947	Burrow
1.598	2.504	7.865	18.82	7.38	0.4836	6.145	2.39	2.55	0.2886	Matrix
1.725	2.511	8.543	20.55	8.68	0.7266	8.505	2.41	2.37	0.501	Burrow
1.927	2.501	9.468	22.65	9.05	0.7311	7.7219	2.39	2.5	0.5309	Burrow
3.565	2.515	17.713	41.33	15.81	1.5344	8.663	2.33	2.61	0.2944	Matrix

The geometric-mean permeability (equation (4)) is that of a homogeneous and isotropic setting where fluid flows in all directions:

$$\ln(k_{\text{geometric}}) = \sum_{i=1}^n \frac{\ln(k_i) d_i}{d} \quad (4)$$

This paper utilizes the concept of Baniak et al. (2015), La Croix et al. (2013), and the three equations to plot graphs of bioturbation intensity (volume of bioturbation from visual assessment) against permeability for core samples. To generate graphs, the three highest permeabilities in burrows (i.e., BI = 6) and the three lowest permeabilities in the matrix (i.e., BI = 0) are averaged to approximate the idealized permeabilities of burrowed and unburrowed endmembers, respectively. This study expresses d_i/d as the volume occupied by burrows in each sample.

3.6. FESEM and EDS

One cubic centimeter (1 cm³) specimens cut from samples are analyzed by Field Emission Scanning Electron Microscopy (FESEM) using the Carl Zeiss Supra 55HKL. This is done to observe their molecular surface structures between 2 Pa and 133 Pa pressures with probe currents from 4 pA to 10 nA. The EDS is further used to analyze specimens for their elemental and chemical properties.

4. Results

4.1. Sedimentary facies and ichnology

Three lithofacies (Lf) each are identified in the E₁f₁ from cored

Table 4
Sample C petrophysical properties (CMS-300 and PDP-200).

Sample	Sample	Sample	Dry	Particle	Pore	Porosity	Vol.	Particle	Permeability	Location
Length	Diameter	Vol.	Wt.	Size	Vol.		Density	Density		
(cm)	(cm)	(cm ³)	(g)	(cm ³)	(cm ³)	(%)	(g/cm ³)	(g/cm ³)	(md)	
4.968	2.552	25.399	63.17	23.47	1.9337	7.6094	2.49	2.69	0.0599	Matrix
4.996	2.538	25.262	62.95	23.55	1.7086	6.7599	2.49	2.67	0.0700	Burrow
4.986	2.526	24.974	63.1	23.64	1.3318	5.3299	2.53	2.67	0.0473	Burrow
4.968	2.528	24.923	62.73	23.58	1.3471	5.4024	2.52	2.66	0.0583	Matrix

Table 5
Distribution of depth, acoustic transit time (Δt), and acoustic porosity (\emptyset) calculated from well H19 acoustic log.

Depth	Δt	Acoustic	Depth	Δt	AC porosity
(m)	(μ sec/ m)	porosity (\emptyset)	(m)	(μ sec/ m)	(\emptyset)
		(%)			(%)
3094.125	331.462	0.33	3095.250	287.606	0.24
3094.250	320.657	0.31	3095.375	292.055	0.25
3094.375	306.674	0.28	3095.500	293.962	0.25
3094.500	297.775	0.26	3095.625	285.064	0.23
3094.625	297.140	0.26	3095.750	281.250	0.23
3094.750	297.140	0.26	3095.875	279.343	0.22
3094.875	293.326	0.25	3096.000	275.530	0.21
3095.000	287.606	0.24	3096.125	269.809	0.20
3095.125	281.250	0.23			

lengths of recurring assemblages and wireline log profiles. About 50 m of 250 cores, 49.6 m of 248 cores, and 48.6 m of 245 cores are described for M7, F12, and H19 wells (Fig. 4). The facies description, facies associations' interpretation, and trace fossils identification are derived from analyzing the wells. Several oil-bearing greyish-green and brownish-red sandstone intervals compose core cuttings in the E_{1f1}, which depict well-conditioned trace fossils and many sedimentary structures. Intense burrowing creates massive or mottled sediments (e.g., Fig. 3O).

Wellbore M7 cored interval description: The lithofacies one (Lf1) 2129–2139 m has intense or completely burrowed ($5 \leq BI \leq 6$; Table 1), well-sorted, oil-stained/bearing yellowish-grey siltstones interlaced with tan mudstones. Trace fossils are *Taenidium* and *Palaeophycus* (e.g., Fig. 3B and E). The lithofacies two (Lf2) 2109–2129 m top succession exhibits single thick-bedded tan mudstone layers about 1 m (1 m), sandwiched between predominant tan siltstones. The bottom-most succession shows well-sorted, parallel-laminated, tan siltstones with fine-grained, well-sorted, parallel-laminated, oil-stained/bearing dark brown sandstones, and massive mudstones. Bioturbation intensity of the observed *Taenidium* and *Palaeophycus* (Fig. 4A) trace fossils are between sparse and intense ($1 \leq BI \leq 5$; Table 1). The lithofacies three (Lf3) 2089–2109 m comprises fine-grained, well-sorted, hummocky (Fig. 3N), and/or cross-stratified brownish-red sandstones and siltstone-intercalated mudstones. The bottom succession shows sedimentary structures obliterated by *Skolithos* (e.g., Fig. 3H), *Palaeophycus*, *Taenidium*, and *Planolites* trace fossils; bioturbation intensity is moderate to intense ($3 \leq BI \leq 5$; Table 1). Sample A is retrieved from this succession (Fig. 4A).

Wellbore F12 cored interval description: The lithofacies one (Lf1) 2094–2104 m has fine-grained, moderately-sorted, cross-stratified, grey sandstones, mottled conglomeratic sandstones, and pebbly gravels (0.5–2 cm). *Beaconites*, *Taenidium*, *Palaeophycus*, and *Skolithos* (e.g., Fig. 3A, C, F, and I), and other simple burrows are dominant with bioturbation intensity between none and high ($0 \leq BI \leq 4$; Table 1). The bottom succession shows, fine-grained, cross-stratified, or mottled yellow sandstones and silty mudstones. The lithofacies two (Lf2) 2074–2094 m has brown siltstones and brown argillaceous siltstones with *Palaeophycus* trace fossils (Fig. 4B). Also, massive, low-angle cross-

bedded, parallel-laminated, and oil-stained/bearing, local current ripple cross-laminated, greyish-green fine-grained sandstones are present (e.g., Fig. 3K-M). Bioturbation is intense or cryptic ($5 \leq BI \leq 6$; Table 1). The bottom succession shows brownish-red fine-grained sandstones. The lithofacies three (Lf3) 2054–2074 m shows brown parallel-laminated siltstones that intersect moderate to intensely burrowed brown siltstones, brown sandstones, and tan mudstones with *Taenidium* and *Palaeophycus* ichnofossils ($0 \leq BI \leq 3$; Table 1); sample B is retrieved from this succession (Fig. 4B). There are sparse to moderately burrowed, muddy tan siltstones, and brownish-red argillaceous siltstones. Trace fossils are subordinate forms of *Taenidium*.

Wellbore H19 cored interval description: The lithofacies one (Lf1) 3094–3104 m displays intensely burrowed, tan mudstones, and cross-stratified argillaceous siltstones intercalated with intensely burrowed, fine-grained, yellowish-grey sandstones ($0 \leq BI \leq 5$; Table 1). Plant debris and/or traces (e.g., Fig. 3G), *Palaeophycus*, and *Planolites* (e.g., Fig. 3D), comprise ichnofossils; sample C is retrieved from this succession (Fig. 4C). The plant debris and/or traces have irregularly distributed features with coaly, sandy, or carbonaceous fills. The underlying succession has conglomeratic tan sandstones about 1.5 m thick. The lithofacies two (Lf2) 3074–3094 m shows conglomeratic, yellowish-grey sandstones and tan mudstones with *Scoyenia* (Fig. 4C). The middle succession has well-sorted, fine-grained, yellowish-grey sandstones with intense or cryptic bioturbation ($5 \leq BI \leq 6$; Table 1). The lithofacies three (Lf3) 3054–3074 m has very fine-grained, tan sandstones, and massive tan mudstones bearing thin-layered silty flow rolls underlain with fine-grained, well-sorted, yellow sandstones. Ichnofossils are *Taenidium* and plant debris and/or traces (Fig. 4C). The extent of bioturbation varies from intense to cryptic ($5 \leq BI \leq 6$; Table 1). Deformed tan mudstones, brown siltstones, and silty mudstones having a bed thickness of about 10.5 m dominate the lowermost succession.

4.2. Reservoir quality in sample A

The average plug volume from the CMS 300 test is 14.39 cm³. Measured porosities range from 3.5% to 10.18% and show the five highest streaks (10.18%, 10.03%, 9.22%, 8.35%, and 8.08%) associated with the bioturbated regions. Burrows and matrix porosities constitute 83.59% and 16.41% of the sample's bulk porosity, respectively. Fig. 5A shows porosity (%) and permeability (0.001 md) distribution. The sample has permeabilities between 0.0091 and 0.0561 md (Table 2; Fig. 5B). Matrix and burrows permeabilities range from 0.0091 to 0.0241 md, and 0.0119 to 0.0561 md, respectively. In Fig. 5C at 0% bioturbation, the lower bounding permeability value is 0.0091 md when 100% fluid flows through the matrix. The upper limit of permeability is 0.0561 md at 100% fluid flow through the most burrowed portions. Sample A is intensely burrowed (BI 5 to 6) by *Palaeophycus*, *Skolithos*, *Scoyenia*, and *Taenidium*. At 100% volume bioturbation (BI = 6), the arithmetic means is 0.024 md (red dot) instead of 0.056 md (green dot; Fig. 5C). Permeability in this sample is numerically closest to and correlates with the arithmetic mean. Matrix and burrow mean permeabilities are 0.02 md and 0.03 md, respectively.

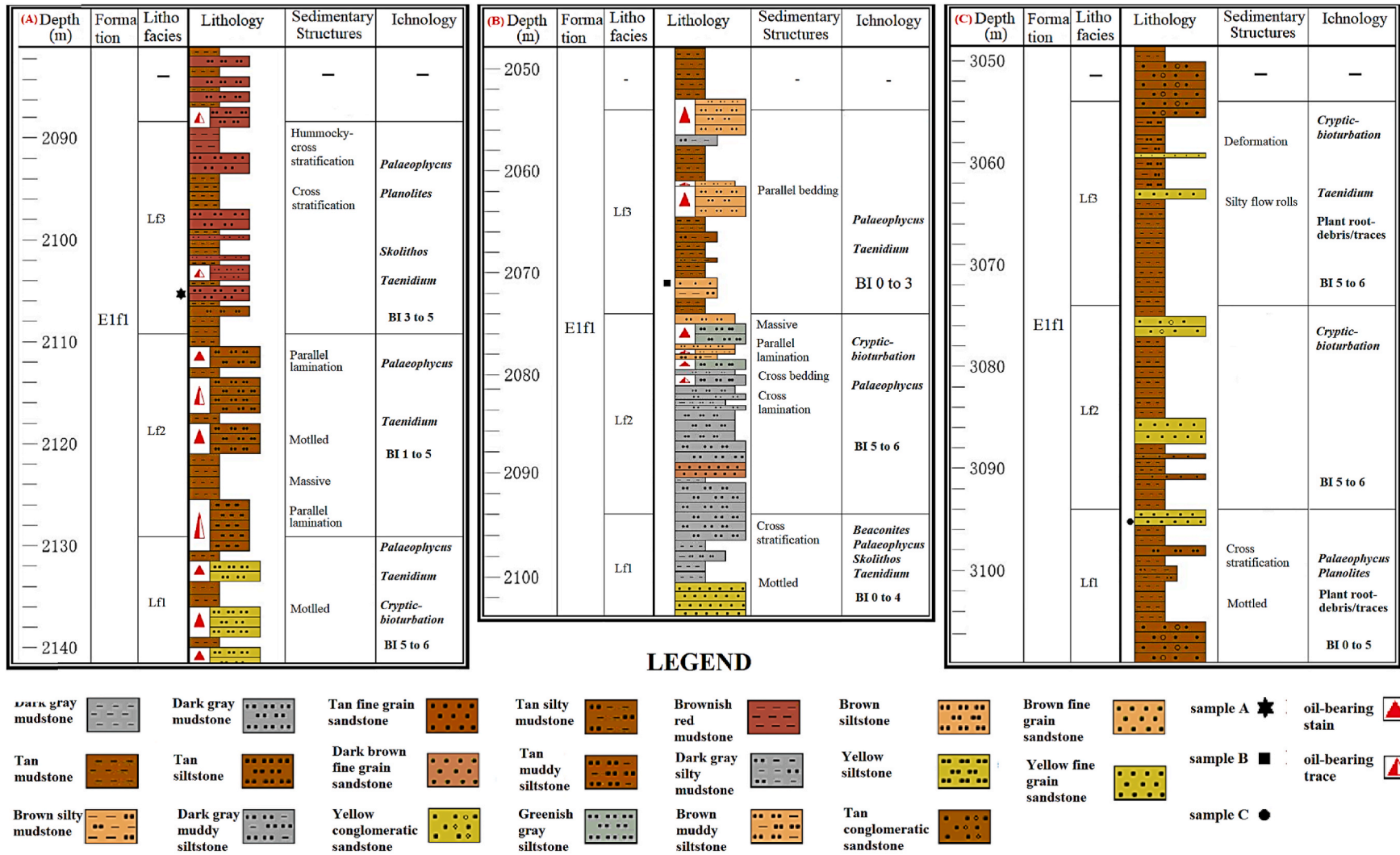


Fig. 4. (A) Wellbore M7 lithology log and associated reservoir facies scheme of a 50 m cored length; (B) Wellbore F12 lithology log and reservoir facies scheme of a 49.6 m cored length; (C) wellbore H19 lithology log and associated reservoir facies scheme of a 48.6 m cored length.

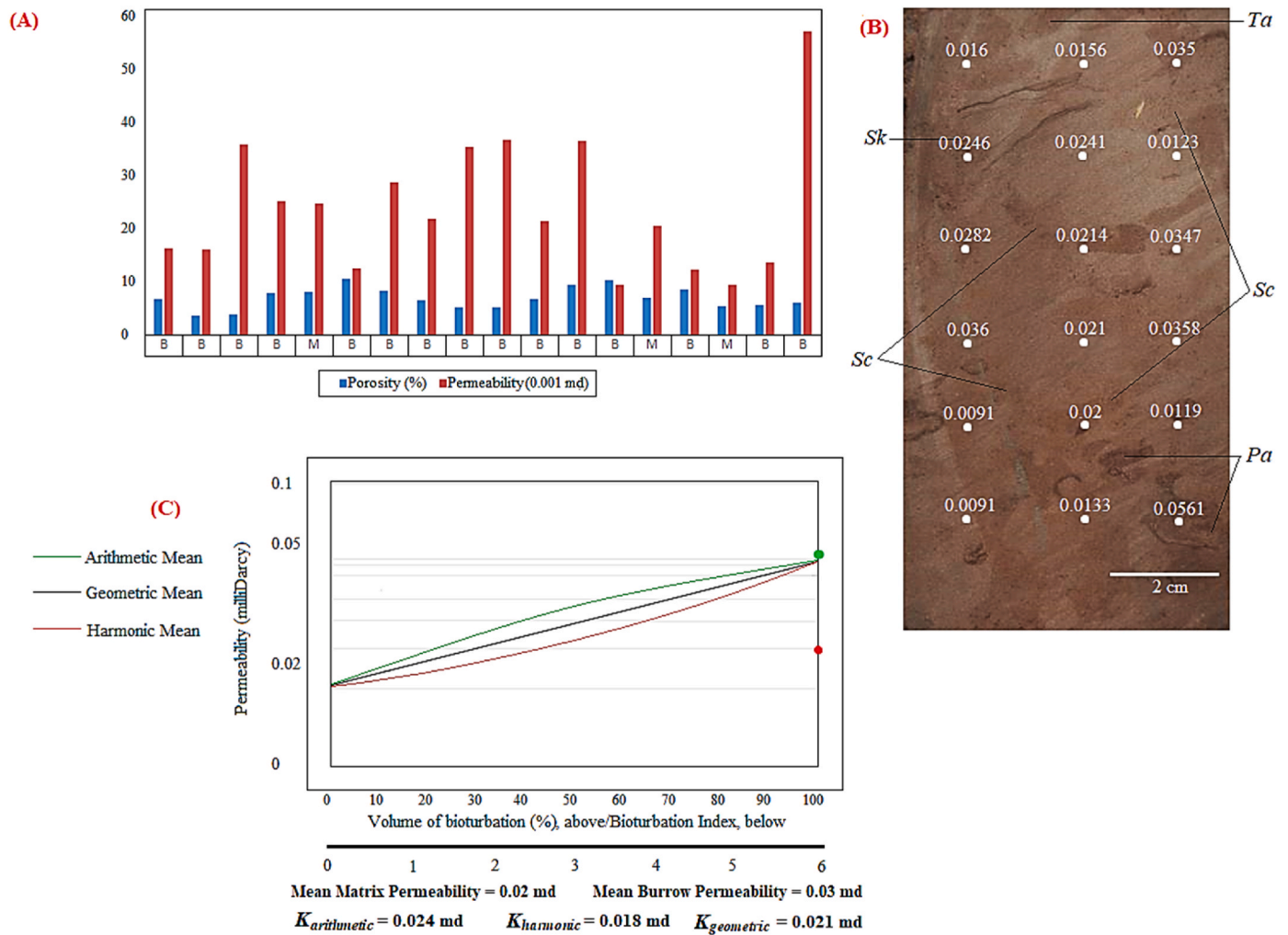


Fig. 5. (A) Sample A two-dimensional clustered column chart showing porosity (%) and permeability (10⁻³ md) distributions; M – Matrix; B – Burrow; (B) PDP-200 permeability data points showing ichnofabrics *Palaeophycus*, *Scoyenia*, *Skolithos*, and *Taenidium*; (C) arithmetic mean best defines permeability (md) (red dot); cryptic bioturbation at 0.024 md instead of the ideal 0.056 md (green dot) at 100% bioturbation. (For interpretation of the references to color in this figure legend, the reader is referred to the Web version of this article.)

4.3. Reservoir quality in sample B

The average plug volume from the CMS 300 test is 11.7 cm³ with porosities ranging from 1.79% to 9.58% (Table 3). The highest and lowest values in the matrix are 9.05% and 1.78%, respectively. Fig. 6A shows porosity (%) and permeability (0.1 md) distribution. Permeability in the sample varies between 0.289 and 0.935 md. Matrix permeabilities are between 0.2886 and 0.935 md whereas burrows permeabilities are between 0.2947 and 0.5309 md (Fig. 6B). At 0% bioturbation, the lower bounding permeability value is 0.2886 md at 100% fluid flow through the matrix.

When fluid flows principally via burrows, when bioturbation is 100%, the permeability upper limit is about 0.531 md. Sample B is highly burrowed (BI = 4) at 85% with the arithmetic mean (red dot) best representing bulk permeability instead of the harmonic mean (green dot). Matrix mean permeability is 0.5 md whereas burrow mean permeability is 0.4 md (Fig. 6C).

4.4. Reservoir quality in sample C

The average plug volume from the CMS 300 test is 25.14 cm³ and porosities range between 5.33% and 7.61%. Matrix and burrows porosities make up 51.84% and 48.16% of the sample's bulk porosity.

Fig. 7A shows porosity (%) and permeability (0.01 md) distribution. Burrows permeabilities are 0.0437md and 0.07 md whereas 0.0583 md and 0.0599 md represent matrix permeabilities; the highest value is associated with the plant debris and/or traces (Fig. 7B and Table 4). At 0% bioturbation and 100% fluid flow through the matrix, the lower limit of permeability is 0.0583 md. When fluid flows mainly through burrows at 100% bioturbation, the permeability upper limit is 0.07 md. The geometric mean of permeability best defines the cryptic nature of burrowing (Baniak et al., 2015). Matrix and burrow mean permeabilities are 0.0591 md and 0.0586 md, respectively (Fig. 7C). From Table 5, the acoustic porosity of the 2 m (i.e., 3094.125–3096.125 m) interval that intersects the position of sample C is between 0.2% and 0.33%. Fig. 8 shows a positive correlation in the graph of acoustic porosity versus acoustic transit time.

4.5. Thin-section petrography, FESEM, and EDS analysis

Sample A burrows show sub-angular to sub-rounded, moderate to well-sorted, and fine grains with discrete boundaries (Fig. 9A and B). The FESEM shows feldspar and cleaner *Taenidium* burrows (Fig. 10A and B).

EDS data shows calcite (CaCO₃) (Ca = 2.2 wt %; C = 18.64 wt %; O = 35.85 wt %), and smaller amounts of quartz (SiO₂) in the matrix (Si =

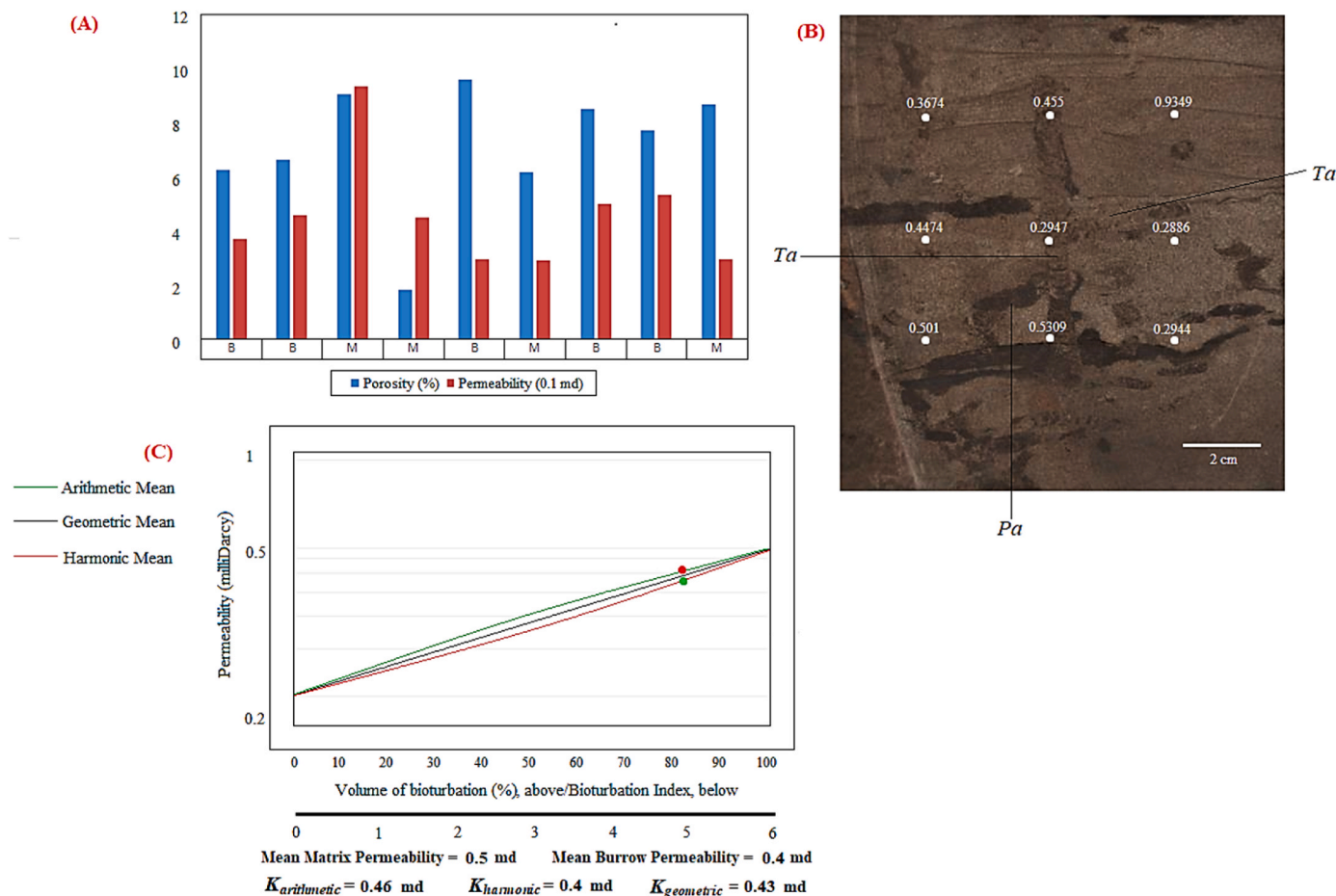


Fig. 6. (A) Sample B two-dimensional clustered column chart showing porosity (%) and permeability (10⁻¹ md) distributions; M – Matrix; B – Burrow; (B) PDP-200 permeability data points showing ichnofabrics *Palaeophycus* and *Taenidium*; (C) arithmetic mean (red dot) best defines permeability instead of the harmonic mean (green dot: 85% bioturbation). (For interpretation of the references to color in this figure legend, the reader is referred to the Web version of this article.)

28.09 wt %; O = 35.85 wt %) than in burrows (Si = 28.41 wt %; O = 48.44 wt %). Smaller quantities of iron oxides (Fe₂O₃) (Fe = 1.13 wt %; O = 48.44 wt %) and relatively larger amounts of feldspar (KAl-Si₃O₈-NaAlSi₃O₈-CaAl₂Si₂O₈) (K = 11.61 wt %; Al = 9.91 wt %; Na = 0.5 wt %; Si = 28.41; O = 48) occur in the matrix (Fig. 11A and B; Table 6A, B).

The *Taenidium* burrow in sample B contains fine-grained, medium to well-sorted, sub-rounded, and sub-angular grains with distinct grain boundaries (Fig. 9C and D). The FESEM in Fig. 10C shows remnants of plagioclase feldspar (albite) around burrows (square inset) after dissolution. The EDS analysis show infiltration of iron oxides (Fe₂O₃) (Fe = 1.37 wt %; O = 58.42 wt %) and clay minerals (e.g., kaolinite; Fig. 10D) in the matrix. The *Taenidium* burrows have no clay minerals but plentiful amounts of quartz (Si = 23.89 wt %; O = 56.88 wt %) and feldspar (K = 0.39 wt %; Al = 10.14 wt %; Na = 6.97 wt %; Ca = 1.72 wt %; Si = 23.89 wt %; O = 56.88 wt %) (Fig. 10C and D; Table 6C, D).

Due to the fine-grained, sub-angular, and sub-rounded grains of quartz and feldspar, sample C exhibits a very high grain density in plant roots debris/traces. The deficiency in cement and noticeable grain edges suggests mechanical compaction is a diagenetic process (Fig. 9E and F). Also, FESEM (Fig. 10E and F) and EDS (Fig. 11E and F) examination show the general composition of the sandstone as quartz and feldspar, whilst EDS data verifies high amounts of clay minerals and iron oxides (Fe₂O₃; Fe = wt. 50.78%; O = wt. 44.21%) in plant debris and/traces (Table 6E, F).

5. Discussion

5.1. Interpretation of facies description

The parallel laminations and low-angle crossbedding in some successions (e.g., lithofacies two of well F12) delineate upper flow regime structures that were created at times of high discharge (Paola et al., 1989; Cheel, 1990; Allen et al., 2011, 2014). The local current ripple cross laminations indicate brief periods of low discharge or reduction in flow intensity (Plink-Björklund, 2015). The parallel-laminated, very fine-grained tan sandstones in the lower succession of well H19 (lithofacies three) show abrupt changes into mottled tan mudstones, which bear local syndepositional structures (e.g., silty flow rolls; Fig. 3J). This implies that the flow intensity sharply reduced; subsequently, suspension or weak currents that formed during the final phase of the flood deposited silt and mud (Miall, 1996; Plink-Björklund, 2015; Horn et al., 2018). The unburrowed, fine-grained sandstones and silty mudstones (e.g., lithofacies one of well F12) are interpreted as a freshwater depositional setting with anoxic conditions (Loucks and Ruppel, 2007). The intensely burrowed facies (e.g., lithofacies one of well M7; lithofacies two of well F12; lithofacies two and three of well H19) are interpreted as extended and intense periods of colonization (Taylor and Goldring, 1993; Gingras et al., 2007). In the upper part of lithofacies, two (lf2) of well F12 and throughout lithofacies three (lf3) of well M7, the producers of *Beaconites*, *Camborygma*, *Palaeophycus*, *Planolites*, *Scoyenia*, *Skolithos*, and *Taenidium* usually colonize the very fine-grained, brownish-red sandstones. The meniscal burrows with brownish-red color represent a subaerial oxidizing environment having a low water table.

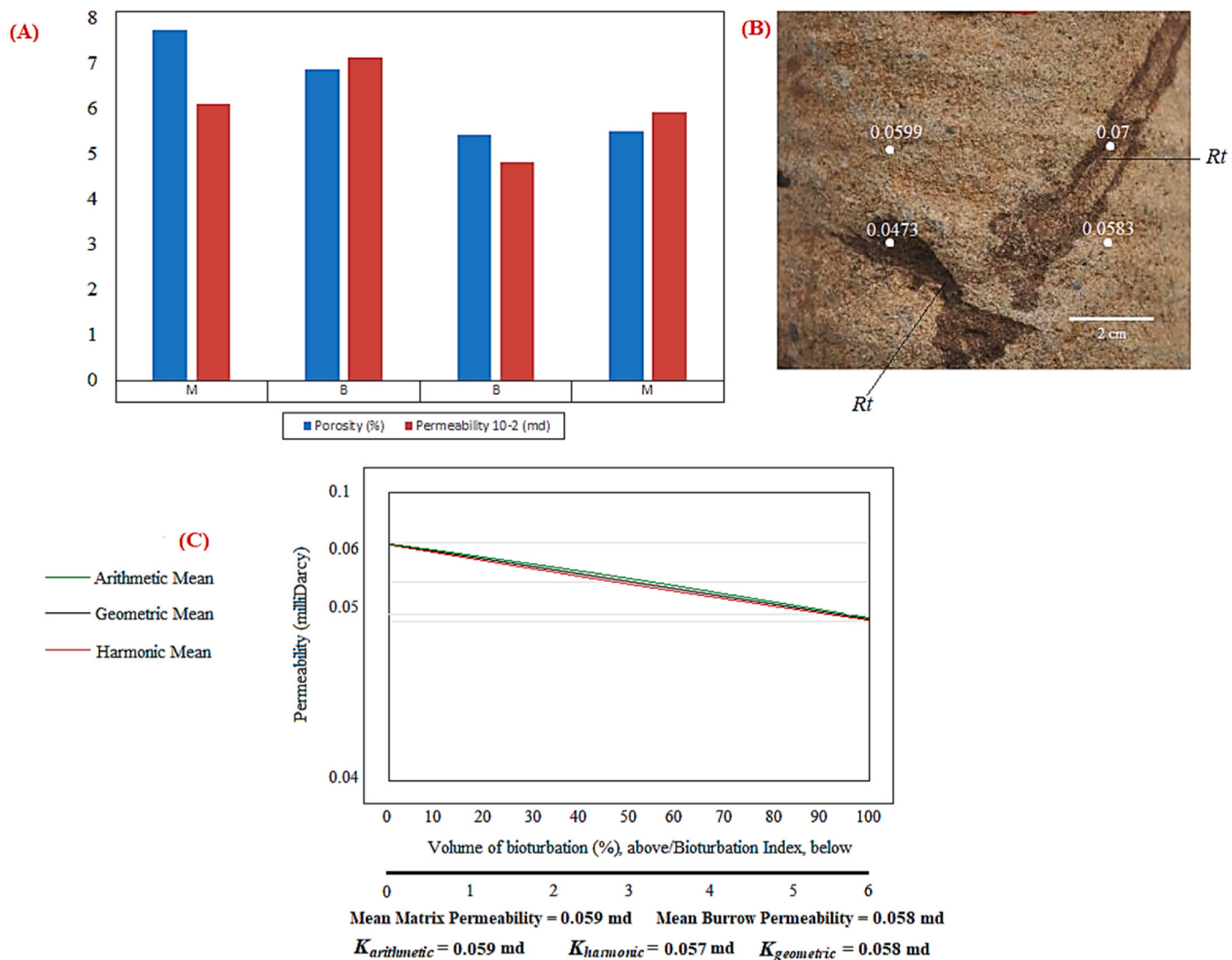


Fig. 7. (A) Sample C two-dimensional clustered column chart showing porosity (%) and permeability (10^{-2} md) distributions; M – Matrix; B – Burrow; (B) PDP-200 permeability data points showing plant debris and/or traces; (C) the geometric mean best defines permeability due to cryptic bioturbation.

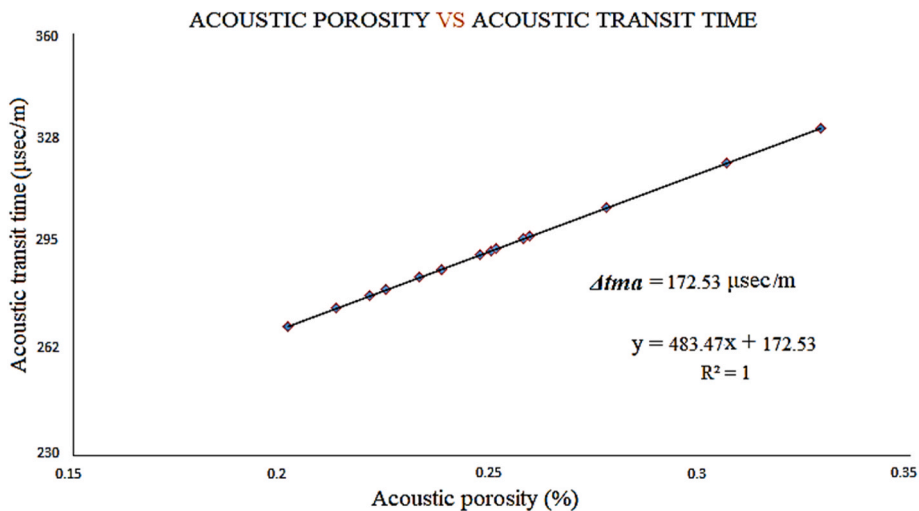


Fig. 8. Graph of acoustic transit time versus acoustic porosity showing a positive correlation; the constant “C” in the equation represents the acoustic transit time of rock matrix (Δt_{ma}) in microsecond/meter.

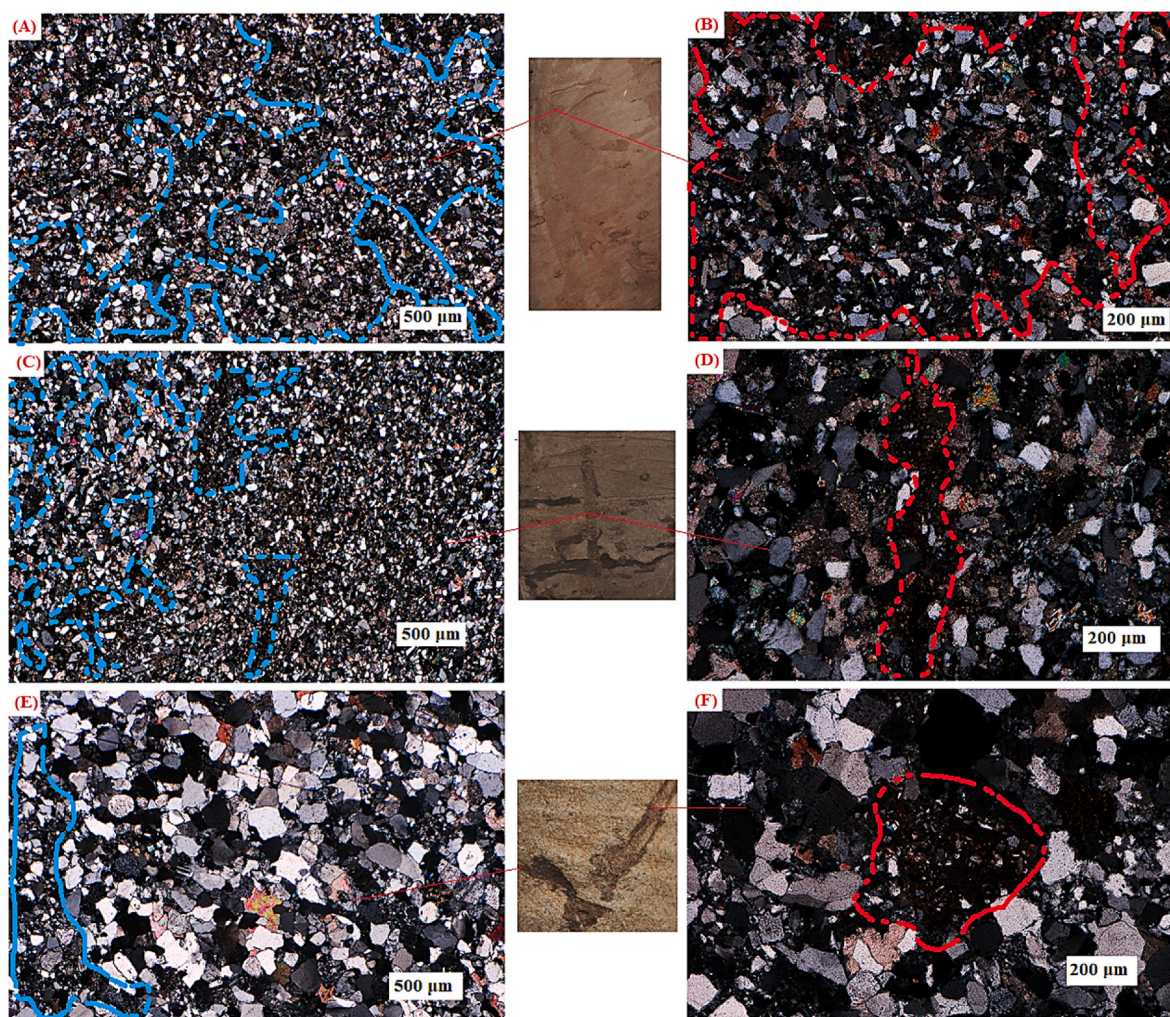


Fig. 9. (A, B) Sample A photomicrographs obtained from the petrographic analysis showing cryptically burrowed portions of siltstone: primary intergranular pore serve as principal reservoir volume (outlined in blue and red dashed lines); (C, D) sample B examples of inter-particle porosity (outlined in blue dashes) in a burrow and medium to well-sorted grains (outlined in red dashes) in *Taenidium* burrow and outlying matrix; (E, F) sample C plant debris and/traces (outlined in blue dashes) showing smaller fine grade grains as compared to the oversized grains in the surrounding matrix; a mixture of mud and fine smaller fine grade material in the presence of iron oxides (delineated in red dashes) in plant debris and/traces. (For interpretation of the references to color in this figure legend, the reader is referred to the Web version of this article.)

To avoid dryness after a channel flood, trace makers of these mineral burrows excavated the moist and soft substrate in search of moisture and food (Hasiotis, 2000; Buatois and Mángano, 2007; Neto De Carvalho et al., 2015). In lithofacies three (lf3) of well M7, hummocky cross-stratifications (HCS) are storm deposits with eroded surfaces showing the storm's height. The cross-stratification indicates a weakening storm whereas the bioturbation and cross lamination illustrate inter-storm idylls (Sellwood, 1990). The landward deposits (e.g. fluvial strata) of HCS by the action of storms (e.g. hurricanes) indicate smaller bedforms due to storm wave attenuation (Woolfe, 1993). Massive or mottled structures are interpreted as events of high sedimentation rate or intense bioturbation (Gingras et al., 2007).

5.2. Evaluation of porosity trends

Diagenetic modifications may contribute significantly to increasing or decreasing reservoir quality (Usman et al., 2020b). From the petrographic analysis of samples A and B at both 200 μm and 500 μm scale levels, dissolution of feldspar mineral occurs (blue and red patches). This contributed to the improvement of porosity in both samples (67.18% in sample A; 20.23% in sample B); the primary intergranular pores serve as the principal reservoir volume (Fig. 9A–D). There is no known study of

Taenidium's effect on reservoir quality; however, moderate to high-density homogeneous fill of burrows, ripple-laminated rocks of different grain size distributions (e.g. an overbank), may assist an enhanced fluid flow response (Knaust, 2017). The albitization of feldspars (Fig. 10B and C) may have had a little positive effect on inter-crystalline micro-porosity in burrows of samples A and B. The kaolinization of alkali feldspars (Fig. 10D) during eodiagenesis reduced inter-crystalline micro-porosity in the matrix of sample B (El-Khatiri et al., 2015). This is shown in the total burrows (83.59% for sample A; 60.11% for sample B) and total matrix (16.41% for sample A; 39.89% for sample B) porosities. The burrows and matrix mean porosities for samples A and B are 6.77% and 6.65% and, 7.73% and 6.41%, respectively. Through the feeding modes of organisms, improved sorting and grain size distribution led to increased isotropy (Quaye et al., 2019), thus enhancing burrows porosity (Tables 2 and 3). The quantities of feldspar and quartz in samples A and B (Fig. 11A–D) suggest that they were formed early and are authigenic. Porosity can be preserved in early-formed authigenic minerals by shielding the rock from subsequent wear through cementation or compaction (Wilson and Pittma, 1977; Anjos et al., 2009). Clay minerals (kaolinite) and iron oxides cleaned from burrows into the matrix of samples A and B suggest there is sediment admixing and/or packing (Tonkin et al., 2010).

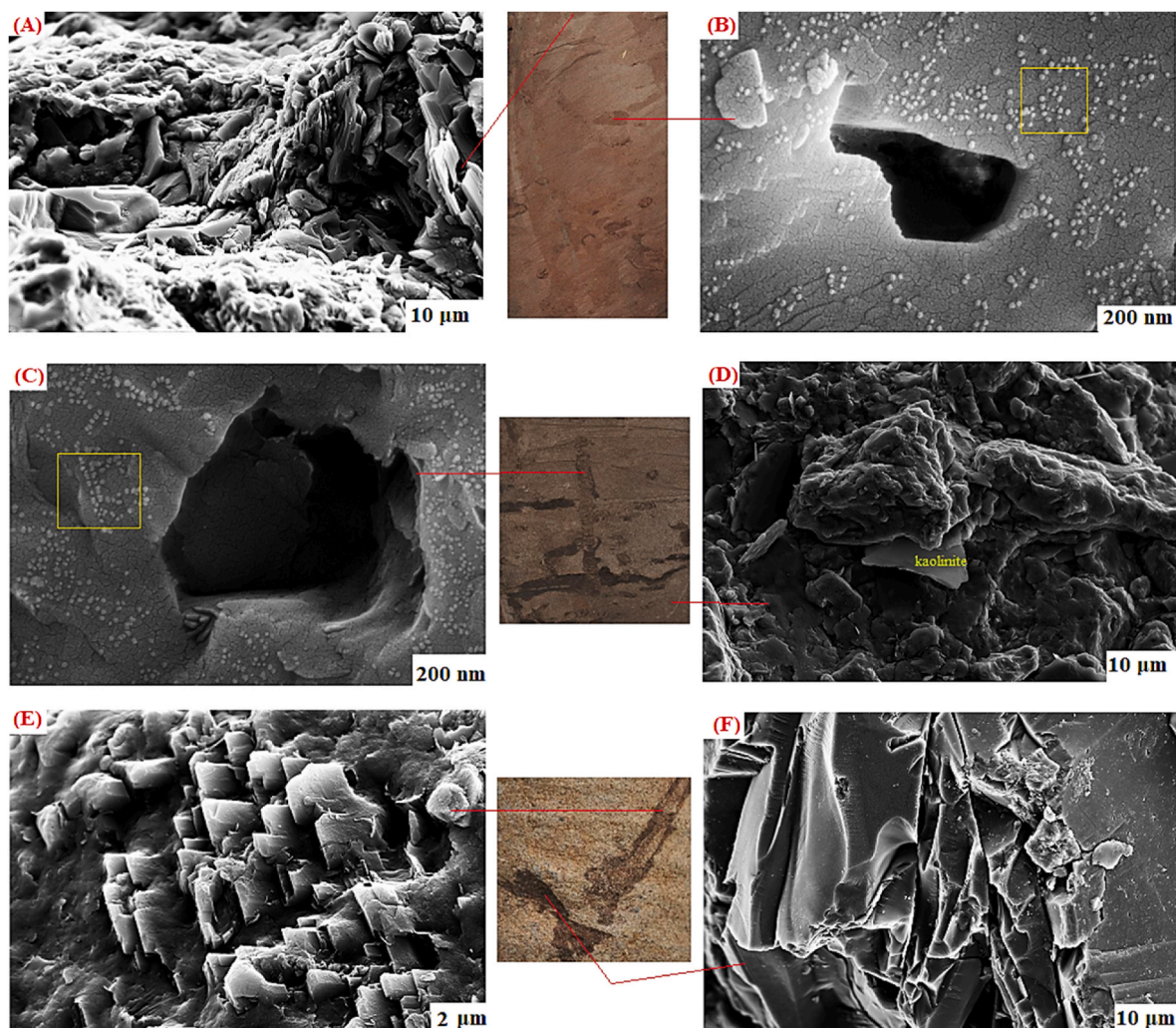


Fig. 10. (A, B) Sample A *Taenidium* burrows FESEM delineating feldspar dominance, and a cleaner burrow with the formation of plagioclase feldspars (albites) remnants on the outlying matrix (square inset) after diagenetic dissolution; (C, D) sample B *Taenidium* burrow FESEM showing albites on the surrounding matrix (square inset), and the unburrowed matrix; (E, F) sample C plant debris and/traces FESEM shows molecular surface structures containing quartz and feldspar.

The disparity between lab-derived and log-derived porosities may be due to several factors existent in the reservoir but absent in the core (e. gs. overburden pressure and compaction). The equation of the straight line in Fig. 7 is expressed as $y = 483.47x + 172.53$ [$\Delta t = (\Delta t_f - \Delta t_m) \phi + \Delta t_m$], where the gradient ($\Delta t_f - \Delta t_m = 483.47$) is the acoustic transit time of interstitial fluids minus acoustic transit time of rock matrix. The y-intercept, Δt_m is 172.53 ($\mu\text{sec}/\text{m}$). The acoustic porosity (ϕ) can be estimated from the equation with known acoustic transit time (Δt). The model is a positive-correlated straight line that shows porosity (ϕ) increases with increasing acoustic transit time ($\mu\text{sec}/\text{m}$).

The precipitation (blue and red patches; Fig. 9E and F) of diagenetic minerals (e.g., feldspar) forms heavy minerals, which reduce porosity and permeability in burrows of sample C. Precipitation of some authigenic minerals (e.g., feldspar) reduces reservoir quality by forming heavier minerals that occupy pore spaces (Wilson and Pittman, 1977). The 7.61% peak porosity is due to sand-filled plant debris and/or traces (Table 4).

For instance, enhanced vertical communication with the reservoir has been documented in sand-filled roots in a tight matrix (Knaust, 2014). The FESEM (Fig. 10E and F) and EDS (Fig. 11E and F) analyses show kaolinite ($\text{Al}_2\text{Si}_2\text{O}_5(\text{OH})_4$) and iron oxides (Fe_2O_3) in burrows affect isotropy and reduce local porosity by 3.68%. In reservoir rocks, iron oxides and clay (Fig. 11E and F) are proofs of sediment mixing and/or packing (e.g., Ben-Awuah and Padmanabhan, 2015).

5.3. Evaluation of permeability trends

Permeability in samples is less than 1 md (Tables 3 and 4), with the lowest values corresponding to argillaceous-dominated and low-bioturbated areas (La Croix et al., 2013). Sample B has higher sand content than sample A, with the highly permeable sections attributed to deposit-feeding (Knaust, 2014; La Croix et al., 2013): feeding on organic and fine-grade material in burrows (Tonkin et al., 2010). From graphs of the volume of bioturbation (%) versus permeability (Figs. 5C and 6C), the curves show a positive correlation, suggesting that highly permeable portions of these samples are most burrowed and act as biogenic micro-fracture systems (Baniak et al., 2013). The arithmetic mean best describes the effective permeability systems in samples A and B. All fluid flow along the most permeable flow pathways is best described by the arithmetic mean (e.g., La Croix et al., 2013).

In sample C, the nature of burrowed sediments has a crucial outcome on permeability because a smaller quantity of fluid flow occurs in burrows due to emplacements of anisotropic units (e.g. clay and iron oxides) (Gingras et al., 1999; Siddiqui et al., 2020). The negative correlation of curves (Fig. 7C) suggests that highly permeable sections of the sample are in the matrix. The fluid flow via the most interconnected flow pathways is described by the geometric mean of permeability. High to intense bioturbation may cause the introduction of clay minerals, however, these clays (e.g. kaolinite) reduce reservoir quality

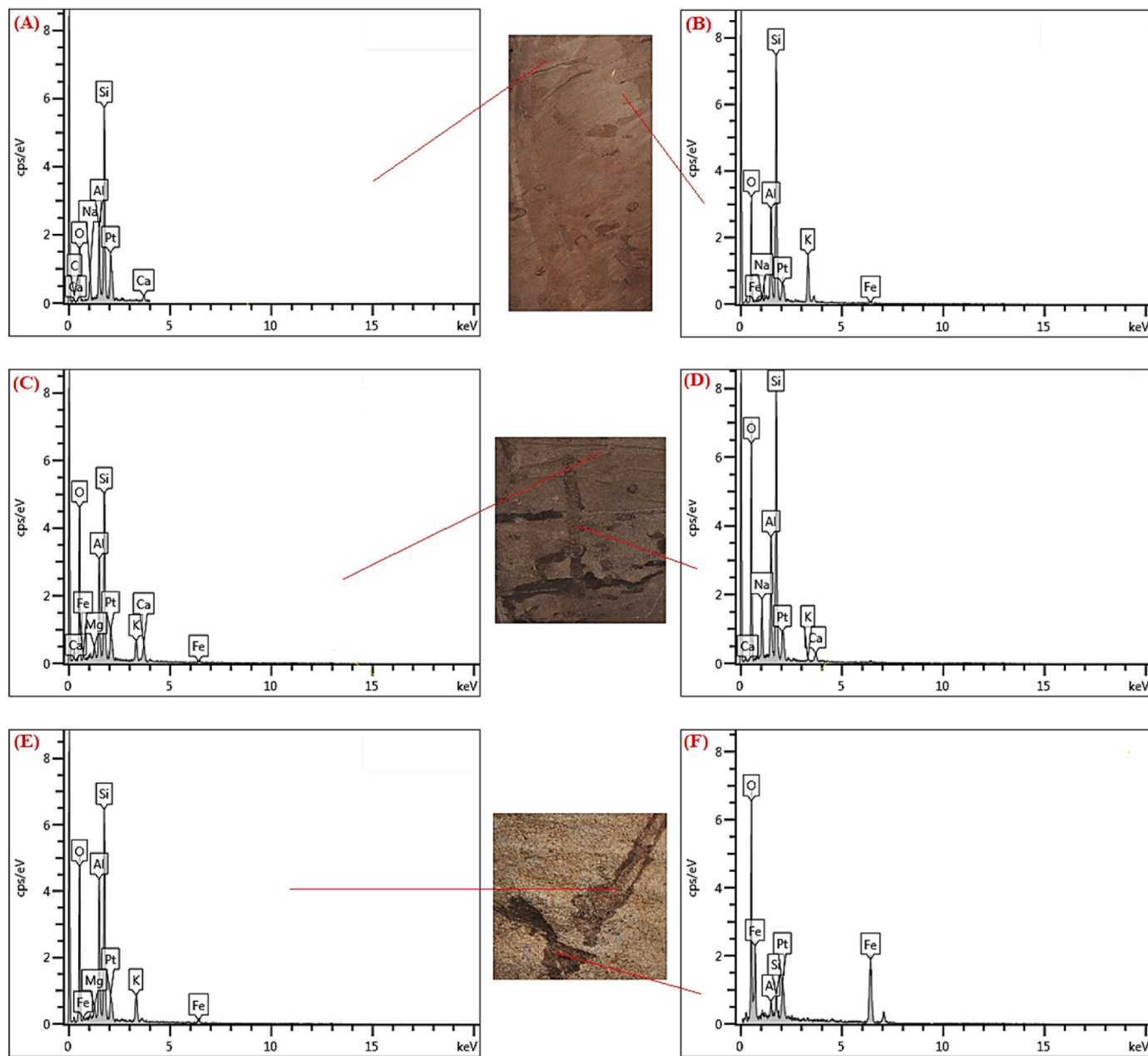


Fig. 11. (A) Sample A *Taenidium* burrow EDS showing calcite and, (B) quartz minerals and surrounding matrix EDS has feldspar and small amounts of iron oxides; (C) Sample B matrix EDS shows feldspar, quartz and clay minerals, and high quantities of iron oxides (D) *Taenidium* burrow EDS showing quartz and feldspar minerals, and (E, F) Sample C plant debris and/trace EDS show quartz, feldspar, clay minerals and moderate to high amounts of iron oxides.

(Anderskov and Surlyk, 2012).

5.4. Evaluation of permeability trends in bioturbated reservoirs

Only the arithmetic and geometric means of permeability are discussed on burrowed facies in E_{1f_1} . The most interconnected and continuous flow networks are defined by the arithmetic mean of permeability. High to intensely bioturbated fabrics that express the *Scoyenia* ichnofacies can be good examples of rock fabrics best characterized by the arithmetic mean of permeability. Proximal denotations of the *Scoyenia* ichnofacies comprise mixtures of clean, silty, and argillaceous substrates that indicate multi-purpose feeding, dwelling, breeding, escape, and scavenging structures (Hubert and Dutcher, 2010) with very high bioturbation intensities. *Palaeophycus*, *Scoyenia*, *Skolithos*, *Taenidium*, and root structures and/or traces comprise common

trace fossils (Zhou et al., 2019). Ubiquitous in continental lacustrine-fluvial sedimentary environments, the *Scoyenia* ichnofacies are oblique to horizontal with bioturbation intensity ranging between high and complete (BI 4 to 6; Knaust, 2017). Ichnofossils such as *Palaeophycus*, *Scoyenia*, and *Taenidium* are fine examples of highly interconnected burrow pathways that are best described by the arithmetic mean of permeability.

The geometric mean best applies to permeability in intervals with extreme bioturbation, and the commonest example in the E_{1f_1} is cryptic bioturbation (see well H19 cored interval; Fig. 4C). In these cryptically-bioturbated intervals, quick and partial or complete overprinting by organisms destroys the burrowed areas, whereas the unburrowed areas appear massive in structure (Gingras et al., 2007). Cryptic bioturbation creates a rather homogeneous flow network. In highly bioturbated systems (herein plants debris and/or traces), many

Table 6

(A, B) Sample A EDS composition from Fig. 10 (A, B); (C, D) sample B EDS composition from Fig. 10 (C, D); (E, F) sample C EDS composition from Fig. 10 (E, F).

(A)	Element	wt. %	wt. % Sigma	Atomic %	(B)	Element	wt. %	wt. % Sigma	Atomic %
	C	18.64	2.14	28.51		O	48.44	0.75	63.8
	O	35.85	1.32	41.15		Na	0.5	0.15	0.46
	Na	5.15	0.32	4.12		Al	9.91	0.29	7.74
	Al	10.07	0.42	6.85		Si	28.41	0.51	21.31
	Si	28.09	0.92	18.37		K	11.61	0.35	6.25
	Ca	2.2	0.25	1.01		Fe	1.13	0.35	0.43
	Total:	100		100		Total:	100		100
(C)	Element	wt. %	wt. % Sigma	Atomic %	(D)	Element	wt. %	wt. % Sigma	Atomic %
	O	58.42	0.66	72.53		O	56.88	0.54	69.2
	Mg	1.1	0.16	0.9		Na	6.97	0.26	5.9
	Al	10.6	0.29	7.8		Al	10.14	0.25	7.32
	Si	19.31	0.4	13.66		Si	23.89	0.38	16.56
	K	4.76	0.25	2.42		K	0.39	0.11	0.19
	Ca	4.45	0.25	2.2		Ca	1.72	0.16	0.84
	Fe	1.37	0.35	0.49		Total:	100		100
	Total:	100		100					
(E)	Element	wt. %	wt. % Sigma	Atomic %	(F)	Element	wt. %	wt. % Sigma	Atomic %
	O	53.53	0.71	68.13		O	44.21	0.9	54.05
	Mg	1.28	0.17	0.46		Al	1.87	0.25	0.65
	Al	13.85	0.35	9.18		Si	3.14	0.25	1.62
	Si	22.86	0.46	15.88		Fe	50.78	0.92	43.68
	K	6.11	0.28	4.38		Total:	100		100
	Fe	2.36	0.38	1.97					
	Total:	100		100					

burrow flow pathways are created both vertical and horizontal, Emplacement of isotropic flow units occur and the geometric mean describes effective permeability, with no preferential fluid flow direction.

6. Conclusions

Three samples burrowed by *Scoyenia* ichnofacies of the lowermost Member Paleocene Funing Formation (E_1f_1), Gaoyou Depression are evaluated to ascertain bioturbation's influence on reservoir quality. Our techniques and analysis of this case study have these conclusions.

1. The increased porosity in burrows of samples A and B rather than in the matrix is based on enhanced isotropy from sediment cleaning activity by burrowing organisms. Clay minerals and/or mud were removed from burrows and deposited in the surrounding matrix.
2. The diagenetic dissolution and albitization of feldspars increase samples A and B burrow intercrystalline micro-porosity. The kaolinization of alkali feldspars in sample B reduces matrix local porosity. Anisotropy, mechanical compaction, and diagenetic precipitation of minerals in sample C reduce reservoir quality.
3. The arithmetic mean best describes the bulk permeability of samples A and B, whereas the geometric mean best characterizes the bulk permeability of sample C. The three values used to calculate the average matrix and burrow permeabilities are within 10–20% of each other. This implies that the “end-member” values used are a good approximation of the samples' permeabilities.

Per the above, we suggest that bioturbation combined with depositional factors (sorting, grain size distribution, and mud-matrix/burrow content) and biogenic diagenetic alterations (albitization, compaction, dissolution, kaolinization, and precipitation) of minerals control reservoir rock quality. Reservoir quality of samples A and B are improved whereas it is reduced in sample C. Consequently, both matrix and burrows in all samples serve as fluid flow units. These findings may be used as a framework to optimize reservoir development in the oil and gas industry.

Credit author statement

Jonathan Ataquaye Quaye: Conceptualization, Writing – original

draft preparation, Writing- Review & editing, Methodology, Software, Data curation, Visualization, Formal analysis, Validation, Zaixing Jiang: Conceptualization, Writing – original draft preparation, Supervision, Project administration, Fund acquisition, Resources, Validation. Chao Liu: Conceptualization, Writing – original draft preparation, Investigation, Software, Validation, Caspar Daniel Adenutsi: Conceptualization, Writing – original draft preparation, Visualization, Investigation, Formal analysis, Validation, Cyril D Boateng: Conceptualization, Writing – original draft preparation, Formal analysis, Validation.

Funding

This research was funded by the China National Science and Technology Major Project (Grant No. 2017ZX05009-002) and the National Natural Science Foundation of China (Grant No. 41772090).

Declaration of competing interest

The authors declare that they have no known competing financial interests or personal relationships that could have appeared to influence the work reported in this paper.

Data availability

Data will be made available on request.

Acknowledgments

We appreciate the contribution of SINOPEC Jiangsu Oilfield Company Ltd to the provision of quality core samples and well data. Many thanks to Journal of Petroleum Science and Engineering editors and reviewers for their constructive remarks that helped identify faults in the paper. Their meticulous comments allowed us to reinforce our research before publication.

References

- Allen, J.P., Fielding, C.R., Gibling, M.R., Rygel, M.C., 2014. Recognizing products of palaeoclimate fluctuation in the fluvial stratigraphic record: an example from the pennsylvanian to lower permian of cape Breton island, Nova scotia. *Sedimentology* 61, 1332–1381. <https://doi.org/10.1111/sed.12102>.

- Allen, J.P., Fielding, C.R., Gibling, M.R., Rygel, M.C., 2011. Fluvial response to paleo-equatorial climate fluctuations during the late Paleozoic ice age. *Bull. Geol. Soc. Am.* 123, 1524–1538. <https://doi.org/10.1130/B30314.1>.
- Anderskov, K., Surlyk, F., 2012. The influence of depositional processes on the porosity of chalk. *J. Geol. Soc. London* 169, 311–325.
- Anjos, S.M.C., De Ros, L.F., Silva, C.M.A., 2009. Chlorite authigenesis and porosity preservation in the upper cretaceous marine sandstones of the Santos basin, offshore eastern Brazil. In: *Clay Mineral Cements in Sandstones*, pp. 289–316. <https://doi.org/10.1002/9781444304336.ch13>.
- Baniak, G., La Croix, A., Gingras, M.K., 2022. Recent Advancements in Characterizing Permeability and Porosity Distributions in Bioturbated Flow Media. <https://doi.org/10.1016/j.earscirev.2022.104162>.
- Baniak, G.M., Gingras, M.K., Burns, B.A., Pemberton, S.G., 2015. Petrophysical characterization of bioturbated sandstone reservoir facies in the upper Jurassic Ula Formation, Norwegian North Sea, Europe. *J. Sediment. Res.* 85, 62–81. <https://doi.org/10.2110/jsr.2015.05>.
- Baniak, G.M., Gingras, M.K., Pemberton, S.G., 2013. Reservoir characterization of burrow-associated dolomites in the upper devonian wabamun Group, pine creek gas field, central Alberta, Canada. *Mar. Petrol. Geol.* 48, 275–292. <https://doi.org/10.1016/j.marpetgeo.2013.08.020>.
- Basilici, G., De Luca, P.H.V., Poire, D.G., 2012. Hummocky cross stratification like structures and combined flow ripples in the Punta Negra Formation (Lower Middle Devonian, Argentine Precordillera): a turbiditic deep water or storm-dominated prodelta inner shelf system? *Sediment. Geol.* 267–268, 73–92. <https://doi.org/10.1016/j.sedgeo.2012.05.012>.
- Bastardie, F., Capowiez, Y., De Dreuzy, J.R., Cluzeau, D., 2003. X-ray tomographic and hydraulic characterization of burrowing by three earthworm species in repacked soil cores. *Appl. Soil Ecol.* 24, 3–16. [https://doi.org/10.1016/S0929-1393\(03\)00071-4](https://doi.org/10.1016/S0929-1393(03)00071-4).
- Ben-awuah, J., Padmanabhan, E., 2015. Effect of bioturbation on reservoir rock quality of sandstones: a case from the Baram Delta, offshore Sarawak, Malaysia. *Petrol. Explor. Dev.* 42, 223–231. [https://doi.org/10.1016/S1876-3804\(15\)30009-4](https://doi.org/10.1016/S1876-3804(15)30009-4).
- Bromley, R.G., Ekdale, A.A., 1984. Chondrites: a trace fossil indicator of anoxia in sediments. *Science* 84 224, 872–874. <https://doi.org/10.1126/science.224.4651.872>.
- Buatois, L.A., Mángano, M.G., 2007. *Trace Fossils: Concepts, Problems, Prospects*. Elsevier, Amsterdam.
- Cheel, R.J., 1990. Horizontal lamination and the sequence of bed phases and stratification under upper flow regime conditions. *Sedimentology* 37, 517–529. <https://doi.org/10.1111/j.1365-3091.1990.tb00151.x>.
- Chen, A.D., 2010. Tectonic features of the Subei basin and the forming mechanism of its dustpan-shaped fault depression. *Oil Gas Geol.* 31, 140–150.
- Dam, G., Andreasen, F., 1990. High-energy ephemeral stream deltas; an example from the upper Silurian holmestrand formation of the oslo region, Norway. *Sediment. Geol.* 66, 197–225. [https://doi.org/10.1016/0037-0738\(90\)90060-7](https://doi.org/10.1016/0037-0738(90)90060-7).
- Deluca, J.L., Eriksson, K.A., 1989. Controls on synchronous ephemeral- and perennial-river sedimentation in the middle sandstone member of the Triassic Chinle Formation, northeastern New Mexico. *U.S.A. Sediment. Geol.* 61, 155–175. [https://doi.org/10.1016/0037-0738\(89\)90056-0](https://doi.org/10.1016/0037-0738(89)90056-0).
- Deng, C., 2014. The Research on Sedimentary Microfacies and Reservoir Characteristic of Elf1 Formation in Gaoji Oilfield, Jinhu Sag. China University of Petroleum (East China), Qingdao, China (in Chinese with English abstract).
- Dey, J., Sen, S., 2017. Impact of bioturbation on reservoir quality and production – a review. *J. Geol. Soc. India* 89, 460–470. <https://doi.org/10.1007/s12594-017-0629-4>.
- Dumas, S., Arnott, R.W.C., Southard, J.B., 2005. Experiments on oscillatory-flow and combined-flow bed forms: implications for interpreting parts of the shallow-marine sedimentary record. *J. Sediment. Res.* 75, 501–513. <https://doi.org/10.2110/jsr.2005.039>.
- El-Khatiri, F., El-Ghali, M.A.K., Mansurbeg, H., Morad, S., Ogle, N., Kalin, R.M., 2015. Diagenetic alterations and reservoir quality evolution of lower cretaceous fluvial sandstones: Nubian formation, Sirt Basin, north-central Libya. *J. Petrol. Geol.* 38, 217–239. <https://doi.org/10.1111/jpg.12607>.
- Freeze, R.A., Cherry, J.A., 1979. *Groundwater*. Prentice-Hall, New Jersey.
- Gang, W.Z., Gao, G., Wang, Y., Shen, X., Gang, W.Z., Gao, G., Wang, Y., Shen, X., 2012. The original Types of Paleogene crude oils in Gaoyou Sag and their migration-accumulation models. *J. Shangdong Univ. Sci. Technol.* 31, 21–28, 2012. 755–784.
- Gao, G., Yang, S., Zhang, W., Wang, Y., Gang, W., Lou, G., 2018. Organic geochemistry of the lacustrine shales from the cretaceous Taizhou Formation in the Gaoyou sag, northern Jiangsu basin. *Mar. Petrol. Geol.* 89, 594–603. <https://doi.org/10.1016/j.marpetgeo.2017.10.023>.
- Gingras, M.K., Bann, K.L., MacEachern, J.A., Pemberton, S.G., 2007. A Conceptual Framework for the Application of Trace Fossils, Applied Ichnology. SEPM Short Course Notes, Tulsa.
- Gingras, M.K., Pemberton, S.G., Mendoza, C.A., Henk, F., 1999. Assessing the anisotropic permeability of Glossifungites surfaces. *Petrol. Geosci.* 5, 349–357. <https://doi.org/10.1144/petgeo.5.4.349>.
- Gordon, J.B., Pemberton, S.G., Gingras, M.K., Konhauser, K.O., 2010. Biogenically enhanced permeability: a petrographic analysis of macaronichnus segregatus in the lower cretaceous Bluesky Formation Alberta Canada. *Am. Assoc. Petrol. Geol. Bull.* 94, 1779–1795. <https://doi.org/10.1306/04061009169>.
- Green, M.A., Aller, R.C., Aller, J.Y., 1992. Experimental evaluation of the influences of biogenic reworking on carbonate preservation in nearshore sediments. *Mar. Geol.* 107, 175–181.
- Gu, Y., Dai, J., 2015. Fault growth and main controlling factors in deep area of Gaoyou Sag. *Geotect. Metallogenia* 39, 53–61.
- Hasiotis, S.T., 2000. The invertebrate invasion and evolution of mesozoic soil ecosystems: the ichnofossil record of ecological innovations. *Paleontol. Soc. Pap.* 6, 141–170. <https://doi.org/10.1017/s1089332600000747>.
- Horn, B.L.D., Goldberg, K., Schultz, C.L., 2018. Interpretation of massive sandstones in ephemeral fluvial settings: a case study from the upper candelária sequence (upper triassic, paraná basin, Brazil). *J. South Am. Earth Sci.* 81, 108–121. <https://doi.org/10.1016/j.jsames.2017.10.009>.
- Hubert, J.F., Dutcher, J.A., 2010. *Scoyenia* escape burrows in fluvial pebbly sand: upper triassic Sugarloaf arkose, deerfield rift basin, Massachusetts, USA. *Ichnos Int. J. Plant Anim* 17, 20–24. <https://doi.org/10.1080/10420940903358529>.
- Jensen, S., Bromley, R.G., 1996. *Trace Fossils. Biology, Taphonomy and Applications*, Second. Geological Magazine. Cambridge University Press, ISBN 0 412 61480 4, p. 361. <https://doi.org/10.1017/s0016756897316987>. London, Glasgow, Weinheim, New York, Tokyo, Melbourne, Madras: Chapman & Hall. Price £24.99 (paperback).
- Jiang, S.L., Nie, H.K., Jing, T.Y., Yu, J.D., Li, M., 2014. Characteristics and oil source comparison of the Funing Formation hydrocarbon source rock in the Gaoyou Sag. *Special Oil Gas Reservoirs* 21, 66–70.
- Katrak, G., Bird, F.L., 2003. Comparative effects of the large bioturbators, *Trypaea australiensis* and *Helocius cordiformis*, on intertidal sediments of Western Port, Victoria, Australia. *Mar. Freshw. Res.* 54, 701–708. <https://doi.org/10.1071/MF03015>.
- Knaust, D., 2017. Atlas of Trace Fossils in Well Core, Atlas of Trace Fossils in Well Core. Springer International Publishing. <https://doi.org/10.1007/978-3-319-49837-9>.
- Knaust, D., 2014. Classification of Bioturbation-Related Reservoir Quality in the Khuff Formation (Middle East): towards a Genetic Approach, pp. 247–267.
- Knight, J., Evans, M., 2017. The sediment stratigraphy of a flood event: an example from the Sabie River, South Africa. *Catena* 151, 87–97. <https://doi.org/10.1016/j.catena.2016.12.015>.
- Konhauser, K.O., Gingras, M.K., 2011. Are animal burrows a major sedimentary sink for metals? *Ichnos Int. J. Plant Anim.* 18, 144–146. <https://doi.org/10.1080/10420940.2011.606517>.
- La Croix, A.D., Gingras, M.K., Pemberton, S.G., Mendoza, C.A., MacEachern, J.A., Lemski, R.T., 2013. Biogenically enhanced reservoir properties in the Medicine Hat gas field, Alberta, Canada. *Mar. Petrol. Geol.* 43, 464–477. <https://doi.org/10.1016/j.marpetgeo.2012.12.002>.
- Leaman, M., McIlroy, D., 2017. Three-dimensional morphological and permeability modelling of *diplocraterion*. *Ichnos Int. J. Plant Anim.* 24, 51–63. <https://doi.org/10.1080/10420940.2016.1232650>.
- Lemski, R.T., Hovikoski, J., Pemberton, S.G., Gingras, M., 2011. Sedimentological, ichnological and reservoir characteristics of the low-permeability, gas-charged Alderson member (Hatton gas field, southwest Saskatchewan): implications for resource development. *Bull. Can. Petrol. Geol.* 59, 27–53. <https://doi.org/10.2113/gscpgbull.59.1.27>.
- Liu, C., Jiang, Z., Zhou, X., Duan, Y., Lei, H., Wang, X., Quaye, J.A., 2021. Paleocene storm-related event beds in the Gaoyou Sag of the Subei Basin, eastern China: a new interpretation for these deep lacustrine sandstones. *Mar. Petrol. Geol.* 124. <https://doi.org/10.1016/j.marpetgeo.2020.104850>.
- Liu, J.H., Tang, J.D., Zhong, S.Y., Yao, F.L., Ge, Z.J., 2012. Sedimentary model of lacustrine carbonate rock in the second member of Funing Formation, the west slope of jinhu sag. *Acta Sedimentol. Sin.* 30, 65–72 (in Chinese with English abstract).
- Liu, Y., Chen, Q., Hu, K., Wang, X., Gao, F., 2014. Comparison of the bohai bay basin and Subei-south Yellow Sea Basin in the structural characteristics and forming mechanism. *Geotect. Metallogenia* 38, 38–51.
- Liu, Y., Chen, Q., Wang, X., Hu, K., Cao, S., Wu, L., Gao, F., 2017. Influence of normal fault growth and linkage on the evolution of a rift basin: a case from the Gaoyou depression of the Subei Basin, eastern China. *Am. Assoc. Petrol. Geol. Bull.* 101, 265–288. <https://doi.org/10.1306/06281615008>.
- Loucks, R.G., Ruppel, S.C., 2007. Mississippian barnett shale: lithofacies and depositional setting of a deep-water shale-gas succession in the foret water basin, Texas. *Am. Assoc. Petrol. Geol. Bull.* <https://doi.org/10.1306/11020606059>.
- Luo, Y.H., Liu, G.L., Liu, J.H., 2013. Productivity characteristics of diamictic reservoir in the second member of Funing Formation of the west slope in Jinhu Sag and its influential factors. *Complex Hydrocarb. Reservoir* 6, 38–40.
- Martin, M.A., Pollard, J.E., 1996. The role of trace fossil (ichnofabric) analysis in the development of depositional models for the Upper Jurassic Fulmar Formation of the Kittiwake Field (Quadrant 21 UKCS). In: *Geology of the Humber Group: Central Graben and Moray Firth*. UKCS, pp. 163–183.
- Meadows, P.S., Tait, J., 1989. Modification of sediment permeability and shear strength by two burrowing invertebrates. *Mar. Biol.* 101, 75–82. <https://doi.org/10.1007/BF00393480>.
- Miall, A.D., 1996. *The Geology of Fluvial Deposits: Sedimentary Facies, Basin Analysis, and Petroleum Geology, the Geology of Fluvial Deposits: Sedimentary Facies, Basin Analysis, and Petroleum Geology*. Springer International Publishing, Berlin. [https://doi.org/10.1016/s0037-0738\(96\)00081-4](https://doi.org/10.1016/s0037-0738(96)00081-4).
- Neto De Carvalho, C., Baucon, A., Canilho, S., Milano, U., 2015. 'meniscate burrow' ichnognid from the alluvial fan deposits of sarzedas basin (upper miocene, Portugal). *Geol. Assoc. Canada* 9, 51–61.
- Over, D.J., 1990. Trace metals in burrow walls and sediments, Georgia Bight, USA. *Ichnos* 1, 31–41. <https://doi.org/10.1080/10420940909386329>.
- Paola, C., Wiele, S.M., Reinhart, M.A., 1989. Upper regime parallel lamination as the result of turbulent sediment transport and low amplitude bed forms. *Sedimentology* 36, 47–59. <https://doi.org/10.1111/j.1365-3091.1989.tb00819.x>.
- Pemberton, S.G., Gingras, M.K., 2005. Classification and characterizations of biogenically enhanced permeability. *Am. Assoc. Petrol. Geol. Bull.* 89, 1493–1517. <https://doi.org/10.1306/07050504121>.

- Petrash, D.A., Lalonde, S.V., Gingras, M.K., Konhauser, K.O., 2011. A surrogate approach to studying the chemical reactivity of burrow mucous linings in marine sediments. *Palaos* 26, 594–600. <https://doi.org/10.2110/palo.2010.p10-140r>.
- Plink-Björklund, P., 2015. Morphodynamics of rivers strongly affected by monsoon precipitation: review of depositional style and forcing factors. *Sediment. Geol.* 323, 110–147. <https://doi.org/10.1016/j.sedgeo.2015.04.004>.
- Qin, X., Tang, J., 2003. Evaluation on the Effect of Low Permeability Reservoir Fracturing and Reforming in Funing Formation in Subei Basin. *China Acad. J. (Electronic Publ. House (in Chinese with English abstract))*.
- Quaye, J.A., Jiang, Z., Zhou, X., 2019. Bioturbation influence on reservoir rock quality: a case study of Well Bian-5 from the second member Paleocene Funing Formation in the Jinhu sag, Subei basin, China. *J. Pet. Sci. Eng.* 172, 1165–1173. <https://doi.org/10.1016/j.petrol.2018.09.026>.
- Renard, P., De Marsily, G., 1997. Calculating equivalent permeability: a review. *Adv. Water Resour.* 20, 253–278. [https://doi.org/10.1016/s0309-1708\(96\)00050-4](https://doi.org/10.1016/s0309-1708(96)00050-4).
- Sellwood, B., 1990. Applied sedimentology, second. In: *Marine and Petroleum Geology*. Academic Press, London. [https://doi.org/10.1016/0264-8172\(90\)90042-f](https://doi.org/10.1016/0264-8172(90)90042-f).
- Shao, X.J., Wang, C.F., Huang, W., Zhong, S.Y., Liu, J.H., Liao, G.M., Chen, J., 2013. Sedimentary characteristics and evolutionary patterns of carbonates in Jinhu depression. Subei Basin. *Shiyou Xuebao/Acta Pet. Sin.* 34, 701–711. <https://doi.org/10.7623/syxb201304010> (in Chinese with English abstract).
- Song, N., Wang, T., Chen, L., Xin, R., 2010. Comprehensive analysis on hydrocarbon accumulation period of upper cretaceous Taizhou Formation in Subei basin. *Shiyou Xuebao/Acta Pet. Sin.* 31, 180–186 (in Chinese with English abstract).
- Tan, D.N.K., Rahman, A.H.B.A., Anuar, A., Bait, B., Chow Kok, Tho, 1999. West Baram delta. In: *The Petroleum Geology and Resources of Malaysia*, pp. 293–341.
- Taylor, A.M., Goldring, R., 1993. Description and analysis of bioturbation and ichnofabric. *J. Geol. Soc.* 150, 141–148. <https://doi.org/10.1144/gsjgs.150.1.0141>.
- Tonkin, N.S., McLroy, D., Meyer, R., Moore-Turpin, A., 2010. Bioturbation influence on reservoir quality: a case study from the cretaceous ben Nevis Formation, Jeanne d'Arc basin, offshore Newfoundland, Canada. *Am. Assoc. Petrol. Geol. Bull.* 94, 1059–1078. <https://doi.org/10.1306/12090909064>.
- Usman, M., Siddiqui, N.A., Mathew, M., Zhang, S., El-Ghali, M.A.K., Ramkumar, M., Jamil, M., Zhang, Y., 2020. Linking the influence of diagenetic properties and clay texture on reservoir quality in sandstones from NW Borneo. *Mar. Petrol. Geol.* 120 <https://doi.org/10.1016/j.marpetgeo.2020.104509>.
- Warren, J.E., Price, H.S., 1961. Flow in heterogeneous porous media. *Soc. Petrol. Eng. J.* 1, 153–169. <https://doi.org/10.2118/1579-g>.
- Weber, K.J., van Geuns, L.C., 1990. Framework for constructing clastic reservoir simulation models. *JPT, J. Pet. Technol.* 42, 1248–1297. <https://doi.org/10.2118/19582-pa>.
- Wilson, M.D., Pittma, E.D., 1977. Authigenic clays in sandstones: recognition and influence on reservoir properties and paleoenvironmental analysis. *SEPM J. Sediment. Res.* 47, 3–31. <https://doi.org/10.1306/212f70e5-2b24-11d7-8648000102c1865d>.
- Woolfe, K.J., 1993. Devonian depositional environments in the Darwin mountains: marine or non-marine? *Antarct. Sci.* 5, 211–220. <https://doi.org/10.1017/S0954102093000276>.
- Xuming, Q., Shiyou, Q., Wenquan, Y., Qidong, L., 2016. Main achievements, new understanding and technological progress for oil and gas exploration in North Jiangsu Basin during the 12th Five-year Plan. *China Pet. Explor.* 21, 62–73.
- Yan, Q., He, Q., 1994. Low Permeability Oilfield Development Technology. *Beijing Pet. Ind. Press (in Chinese with English abstract)*.
- Yang, Q., Chen, H.Y., 2003. Tectonic evolution of the north jiangsu–south Yellow Sea basin. *Pet. Geol. Exp.* 25, 562–565. <https://doi.org/10.3969/j.issn.1001-6112.2003.z1.008>.
- Yi, S., Yi, S., Batten, D.J., Yun, H., Park, S.J., 2003. Cretaceous and cenozoic non-marine deposits of the northern south Yellow Sea basin, offshore western korea: palynostratigraphy and palaeoenvironments. *Palaeogeogr. Palaeoclimatol. Palaeoecol.* 191, 15–44. [https://doi.org/10.1016/S0031-0182\(02\)00637-5](https://doi.org/10.1016/S0031-0182(02)00637-5).
- Zhang, J.L., Si, X.Q., Lin, H., 2006. Sedimentary facies analysis of the 3rd member of the Funing Formation in the jinhu depression. *Period. Ocean Univ. China* 36, 535–539 (in Chinese with English abstract).
- Zhang, X.L., Zhu, X.M., Zhong, D.K., Liang, B.G., Cao, B., He, X.Y., 2004. The character of sequence framework of tertiary and upper cretaceous in Gaoyou sag, northern Jiangsu Basin. *Acta Sedimentol. Sin.* 22, 393–399 (in Chinese with English abstract).
- Zhou, X., Jiang, Z., Quaye, J.A., Duan, Y., Hu, C., Liu, C., Han, C., 2019. Ichnology and sedimentology of the trace fossil-bearing fluvial red beds from the lowermost member of the Paleocene Funing Formation in the jinhu depression, Subei basin, east China. *Mar. Petrol. Geol.* 99, 393–415. <https://doi.org/10.1016/j.marpetgeo.2018.10.032>.
- Zhu, G., Jiang, Q.Q., Piao, X.F., Xie, C.L., 2013. Role of basement faults in faulting system development of a rift basin: an example from the Gaoyou Sag in Southern Northern Jiangsu Basin. *Acta Geol. Sin.* 87, 441–452.